Neuron

Article

Microglial $P2Y_6$ calcium signaling promotes phagocytosis and shapes neuroimmune responses in epileptogenesis

Graphical abstract

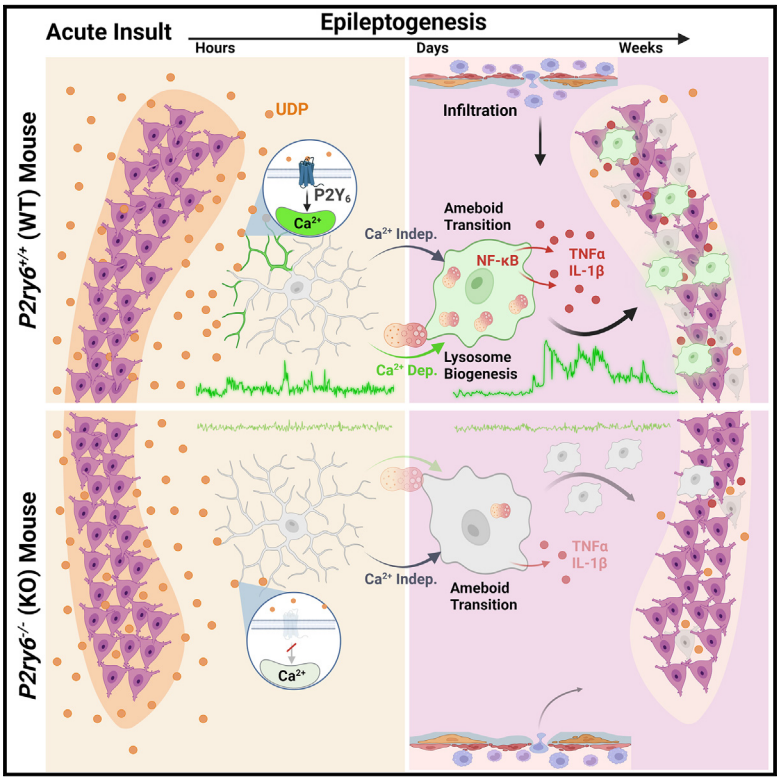

Highlights

- A UDP1.0 sensor reports enhanced UDP release following hyperexcitability
- UDP-$P2Y_6$ signaling transduces microglial calcium activity in epileptogenesis
- $P2Y_6$ signaling enhances lysosome biogenesis and inflammatory cytokine production
- Preventing $P2Y_6$ signaling preserves neurons and cognition

Authors

Anthony D. Umpierre, Bohan Li, Katayoun Ayasoufi, ..., Aaron J. Johnson, Yulong Li, Long-Jun Wu

Correspondence

umpierre.anthony@mayo.edu (A.D.U.), yulongli@pku.edu.cn (Y.L.), longjun.wu@uth.tmc.edu (L.-J.W.)

In brief

Umpierre, Li, et al. demonstrate that post-seizure UDP release can activate microglial calcium activity through the $P2Y_6$ receptor. UDP-$P2Y_6$ signaling engages multiple aspects of immune function during early epilepsy development, including engulfment of neuronal somata and pro-inflammatory cytokine production. $P2Y_6$ deficiency attenuates pyramidal cell loss and cognitive impairment.

Umpierre et al., 2024, Neuron *112*, 1–19
June 19, 2024
https://doi.org/10.1016/j.neuron.2024.03.017

CellPress

Please cite this article in press as: Umpierre et al., Microglial $P2Y_6$ calcium signaling promotes phagocytosis and shapes neuroimmune responses in epileptogenesis, Neuron (2024), https://doi.org/10.1016/j.neuron.2024.03.017

Neuron

CellPress

Article

Microglial $P2Y_6$ calcium signaling promotes phagocytosis and shapes neuroimmune responses in epileptogenesis

Anthony D. Umpierre,[1,10,*] Bohan Li,[2,10] Katayoun Ayasoufi,[3] Whitney L. Simon,[4] Shunyi Zhao,[1,4] Manling Xie,[1] Grace Thyen,[1] Benjamin Hur,[5,6] Jiaying Zheng,[1] Yue Liang,[1] Dale B. Bosco,[1] Mark A. Maynes,[4] Zhaofa Wu,[2] Xinzhu Yu,[7] Jaeyun Sung,[5,6] Aaron J. Johnson,[1,3] Yulong Li,[2,*] and Long-Jun Wu[1,3,8,9,11,*]

[1]Department of Neurology, Mayo Clinic, Rochester, MN 55905, USA
[2]State Key Laboratory of Membrane Biology, Peking University School of Life Sciences, Beijing 100871, China
[3]Department of Immunology, Mayo Clinic, Rochester, MN 55905, USA
[4]Graduate School of Biomedical Sciences, Mayo Clinic, Rochester, MN 55905, USA
[5]Center for Individualized Medicine, Mayo Clinic, Rochester, MN 55905, USA
[6]Department of Surgery, Mayo Clinic, Rochester, MN 55905, USA
[7]Department of Molecular and Integrative Physiology, University of Illinois at Urbana-Champaign, Urbana, IL 61801, USA
[8]Center for Neuroimmunology and Glial Biology, Institute of Molecular Medicine, University of Texas Health Science Center, Houston, TX 77030, USA
[9]Present address: Center for Neuroimmunology and Glial Biology, Institute of Molecular Medicine, University of Texas Health Science Center, Houston, TX, USA
[10]These authors contributed equally
[11]Lead contact
*Correspondence: umpierre.anthony@mayo.edu (A.D.U.), yulongli@pku.edu.cn (Y.L.), longjun.wu@uth.tmc.edu (L.-J.W.)
https://doi.org/10.1016/j.neuron.2024.03.017

SUMMARY

Microglial calcium signaling is rare in a baseline state but strongly engaged during early epilepsy development. The mechanism(s) governing microglial calcium signaling are not known. By developing an *in vivo* uridine diphosphate (UDP) fluorescent sensor, $GRAB_{UDP1.0}$, we discovered that UDP release is a conserved response to seizures and excitotoxicity across brain regions. UDP can signal through the microglial-enriched $P2Y_6$ receptor to increase calcium activity during epileptogenesis. $P2Y_6$ calcium activity is associated with lysosome biogenesis and enhanced production of NF-κB-related cytokines. In the hippocampus, knockout of the $P2Y_6$ receptor prevents microglia from fully engulfing neurons. Attenuating microglial calcium signaling through calcium extruder ("CalEx") expression recapitulates multiple features of $P2Y_6$ knockout, including reduced lysosome biogenesis and phagocytic interactions. Ultimately, $P2Y_6$ knockout mice retain more CA3 neurons and better cognitive task performance during epileptogenesis. Our results demonstrate that $P2Y_6$ signaling impacts multiple aspects of myeloid cell immune function during epileptogenesis.

INTRODUCTION

Patterns of microglial calcium activity are fundamentally different from local astrocytes or neurons. Microglia rarely display spontaneous calcium activity in a naive state[1–3] but are known to elevate their calcium signaling following CNS injury, inflammation, or hyperactivity.[2–5] Therein, microglial calcium signaling could play a role in coordinating pathological responses, including neuroimmune functions.[6,7]

The early phase of epilepsy development ("epileptogenesis") represents an ideal context to study microglial calcium signaling, including its mechanism(s), role in injury response, and potential impact on disease progression. Epileptogenesis, when modeled by the systemic administration of kainate (KA), induces a prolonged seizure state known as status epilepticus (SE or KA-SE). KA-SE results in cell death,[8–10] gliosis,[8,9] and network rearrangement.[11,12] Following SE, microglia display prolonged, whole-cell calcium transients[3] over a 2-week period.

We hypothesize that microglial calcium elevations in epileptogenesis are driven by purinergic signaling. Purines are released during periods of damage, inflammation, and hyperexcitability, with the ability to evoke calcium signaling in most cell types.[13–18] In other electrically non-excitable cells, like astrocytes, large calcium transients are often ascribed to $G_{\alpha q}$-PLC-IP_3 metabotropic pathway activation.[19–21] According to transcriptomic databases,[22] only one purine-sensitive receptor, $P2Y_6$, is linked to an intracellular $G_{\alpha q}$-PLC-IP_3 calcium pathway in microglia. The $P2Y_6$ receptor is highly enriched in microglia and other myeloid

Please cite this article in press as: Umpierre et al., Microglial P2Y$_6$ calcium signaling promotes phagocytosis and shapes neuroimmune responses in epileptogenesis, Neuron (2024), https://doi.org/10.1016/j.neuron.2024.03.017

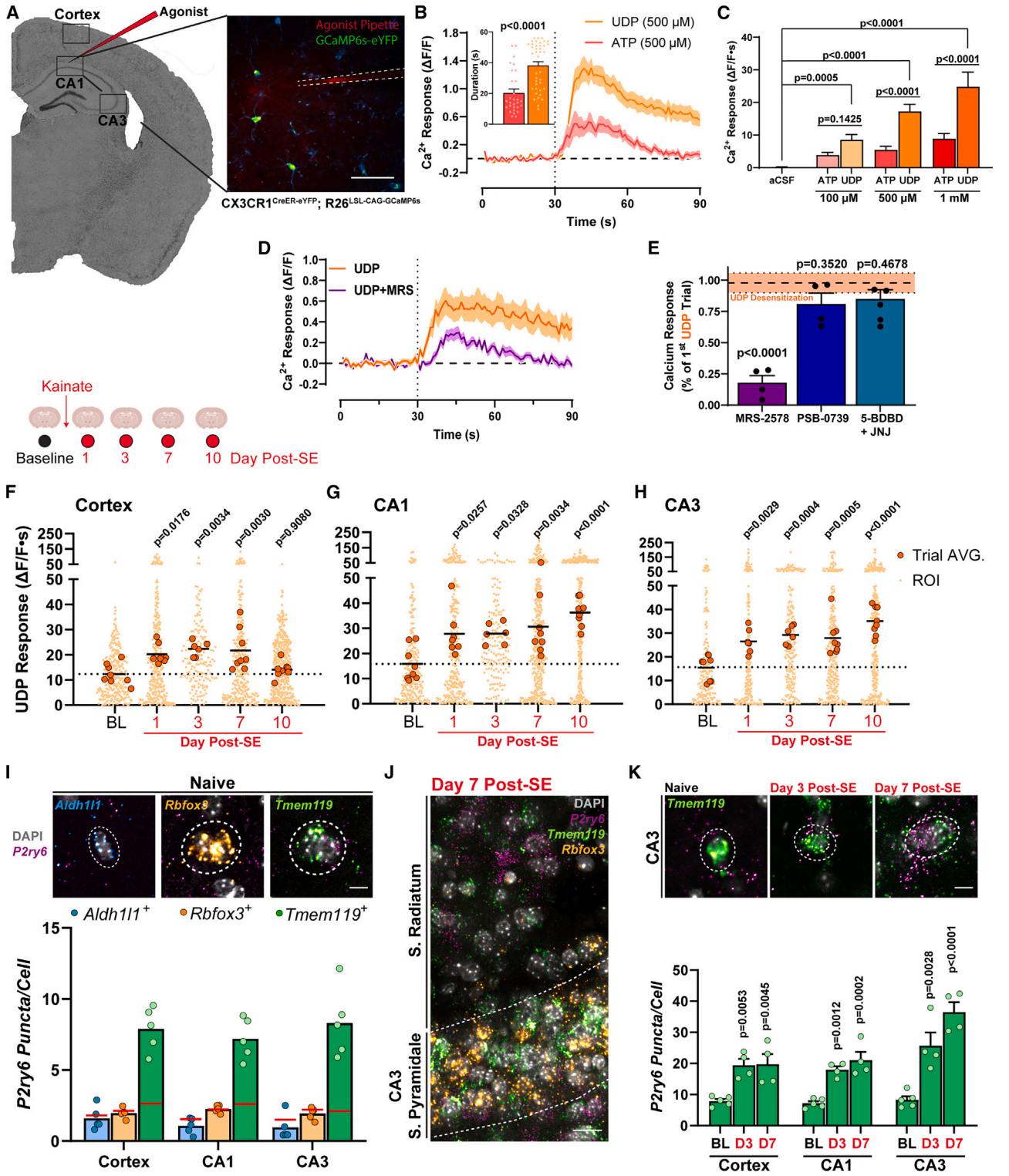

Figure 1. UDP engages microglial calcium signaling through P2Y$_6$ receptors, with enhanced sensitivity during epileptogenesis

(A) Image of an acute brain slice expressing GCaMP6s in microglia. Scale bar, 100 μm.

(B) Microglial calcium responses to ATP or UDP application (whole-cell regions of interest [ROIs]). Inset: response duration (n = 3 mice; unpaired t test).

(C) Overall calcium responses to aCSF or purine application. Two-way ANOVA with Dunnett's post hoc comparison to aCSF or Sidak's post hoc test (UDP vs. ATP; 4–6 slices from n = 3–4 mice).

(legend continued on next page)

Please cite this article in press as: Umpierre et al., Microglial $P2Y_6$ calcium signaling promotes phagocytosis and shapes neuroimmune responses in epileptogenesis, Neuron (2024), https://doi.org/10.1016/j.neuron.2024.03.017

cells.[23] In the brain, its expression is restricted to microglia and a subset of hypothalamic neurons.[24,25] $P2Y_6$ has its highest endogenous affinity for the pyrimidine uridine diphosphate (UDP), which is known to be elevated during epileptogenesis.[24]

We investigated how UDP-$P2Y_6$ signaling influences microglial calcium signaling and cellular function during epileptogenesis. We developed a novel UDP fluorescent sensor, $GRAB_{UDP1.0}$, to visualize real-time UDP signaling in the mouse brain. Enhanced UDP release occurs across multiple brain regions in early epileptogenesis. Loss of the UDP-sensitive $P2Y_6$ pathway strongly attenuates spontaneous microglial calcium signaling during epileptogenesis and is associated with reduced pro-inflammatory cytokine production, deficits in microglial phagocytosis, and enhanced CA3 neuron survival.

RESULTS

UDP evokes calcium activity in microglia, with enhanced sensitivity during epileptogenesis

UDP may engage calcium signaling in microglia, based upon its activation of the $G_{\alpha q}$-linked $P2Y_6$ receptor. In a naive state, we can detect microglial calcium responses to UDP in the range of 100 μM to 1 mM ($Cx3Cr1^{CreER\text{-}IRES\text{-}eYFP}$; $R26^{LSL\text{-}CAG\text{-}GCaMP6s}$ acute brain slice; Figures 1A–1C). ATP calcium responses are notably shorter in duration and smaller in magnitude (Figures 1B and 1C). UDP application predominately transduces calcium signaling in microglia via $P2Y_6$ receptors, as the selective antagonist MRS-2578 (40 μM) reduces UDP responses by 82.1% ± 5.8% (Figures 1D and 1E). UDP has minimal calcium activity at other purine receptors, including $P2X_4$/$P2X_7$ and $P2Y_{12}$, based upon antagonist studies (Figure 1E). Pharmacological studies therefore suggest that UDP could promote calcium activity in microglia at micromolar levels via $P2Y_6$ receptor activation.

$P2Y_6$ expression in microglia can be upregulated following brain insults.[23] As previously noted,[24–26] *P2ry6* is largely enriched in microglia (*Tmem119*$^+$ cells) in the naive brain compared with astrocytes (*Aldh1l1*$^+$ cells) or NeuN neurons (*Rbfox3*$^+$ cells; Figure 1I). The number of *P2ry6* mRNA puncta surrounding astrocytes and neurons in wild-type (WT) tissue was not statistically distinguishable from negative control values (Figure 1I). During epileptogenesis, *Tmem119*$^+$ microglia have increased *P2ry6* puncta levels 3 and 7 days after KA-SE in the cortex, CA3, and CA1 regions (Figures 1J and 1K). Elevated *P2ry6* transcript levels are temporally associated with periods in which microglia have increased calcium responses to UDP (Figures 1F–1H). Collectively, these results suggest that microglia have enhanced *P2ry6* transcription and heightened UDP calcium sensitivity during epileptogenesis.

Development of a fluorescent sensor for *in vivo* imaging of extracellular UDP

To determine whether UDP could serve as an endogenous activator of microglial calcium signaling during epileptogenesis, we developed a high-performance, G-protein-coupled receptor (GPCR)-activation-based (GRAB) sensor to visualize UDP release. To engineer a UDP sensor, we inserted a circularly permutated, enhanced GFP (cpEGFP) molecule between transmembrane domains 5 and 6 of the chicken $P2Y_6$ ($cP2Y_6$) receptor, using flanking linker sequences derived from $GRAB_{NE1m}$[26] to form a modified intracellular loop (Figure 2A). By optimizing linker sequence length and residue composition, we produced a candidate sensor with strong fluorescent responses to UDP, which we termed $GRAB_{UDP1.0}$, or UDP1.0 (Figures 2B, S1A, and S1B). In HEK293T cells, UDP1.0 is properly trafficked to the plasma membrane (Figure S1C) and displays an approximate 6-fold ΔF/F response to 10 μM UDP (Figures 2C and 2D). Its single-photon excitation and emission spectra are similar to EGFP (Figure 2E). Non-selective P2Y receptor antagonists Suramin and PPADS can disrupt UDP1.0 fluorescent responses to UDP (Figure 2F). The sensor displays strong selectivity for UDP over other purines/pyrimidines and neurotransmitters (Figure 2F). After UDP, uridine triphosphate (UTP) has the next highest affinity for the sensor with a 16-fold difference in EC_{50} value (Figure 2G). We additionally examined whether UDP1.0 would couple to a native $G_{\alpha q}$ pathway (split-luciferase complementation assay; Figure 2H). Similar to non-transfected cells, UDP1.0 exhibits minimal $G_{\alpha q}$-dependent coupling (vs. the WT $cP2Y_6$ receptor; Figure 2H), with similar results obtained in calcium mobilization assays (Figures S1D–S1F). In addition, the sensor is unlikely to undergo internalization, as 2-h incubation with 100 μM UDP does not significantly reduce sensor fluorescence over time (Figure 2I). *In vitro* characterization demonstrates that UDP1.0 can detect UDP in the nanomolar to micromolar range with strong selectivity over all other ligands tested.

We further evaluated UDP1.0 signal dynamics in acute brain slices with viral delivery (AAV2/9-hSyn-UDP1.0; Figures 2J–2L). Exogenous UDP application can evoke sensor responses as low as 500 nM in acute brain slices. However, UDP responses are best observed in a dynamic range between 10 and 250 μM (Figure 2L). By contrast, sensor responses to ATP, ADP, and UTP are distinctly smaller than UDP responses in the same concentration range (Figures 2K and 2L). Therein, UDP1.0 can also function with reasonable selectivity for UDP over other purines/pyrimidines in brain tissue.

(D) Calcium responses to UDP alone or in a paired trial with a $P2Y_6$ antagonist (MRS-2578).
(E) Effects of antagonists on UDP calcium responses (dot, paired trial; n = 4). One-way ANOVA with Dunnett's post hoc comparison to desensitization (orange horizontal line; see STAR Methods).
(F–H) Microglial whole-cell calcium responses to 500 μM UDP application in cortex (F), CA1 (G), or CA3 (H) (2 slices per mouse, n = 3–4). One-way ANOVA with Dunnett's post hoc comparison to baseline (trial average data).
(I) Top: images of *P2ry6* puncta near *Aldh1l1*, *Rbfox3*, or *Tmem119* nuclei. Scale bar, 5 μm. Bottom: quantification of *P2ry6* puncta near different cell types (n = 5 naive C57 WT mice). The red line represents a negative control (false inclusion) threshold (see STAR Methods).
(J) Representative *in situ* hybridization image from the CA3 region 7 days after KA-SE. Scale bar, 25 μm.
(K) Top: *P2ry6* mRNA near *Tmem119*$^+$ nuclei in the CA3 across time points. Scale bar, 5 μm. Bottom: quantification of *P2ry6* puncta across time points. One-way ANOVA with Dunnett's post hoc comparison to baseline for each region (n = 5 naive WT mice and n = 4 WT mice day 3 and day 7).
Bar or line graphs, mean ± SEM; small dots, individual ROIs (B and F–H); large circles, slice/tissue average (F–K).

Please cite this article in press as: Umpierre et al., Microglial P2Y$_6$ calcium signaling promotes phagocytosis and shapes neuroimmune responses in epileptogenesis, Neuron (2024), https://doi.org/10.1016/j.neuron.2024.03.017

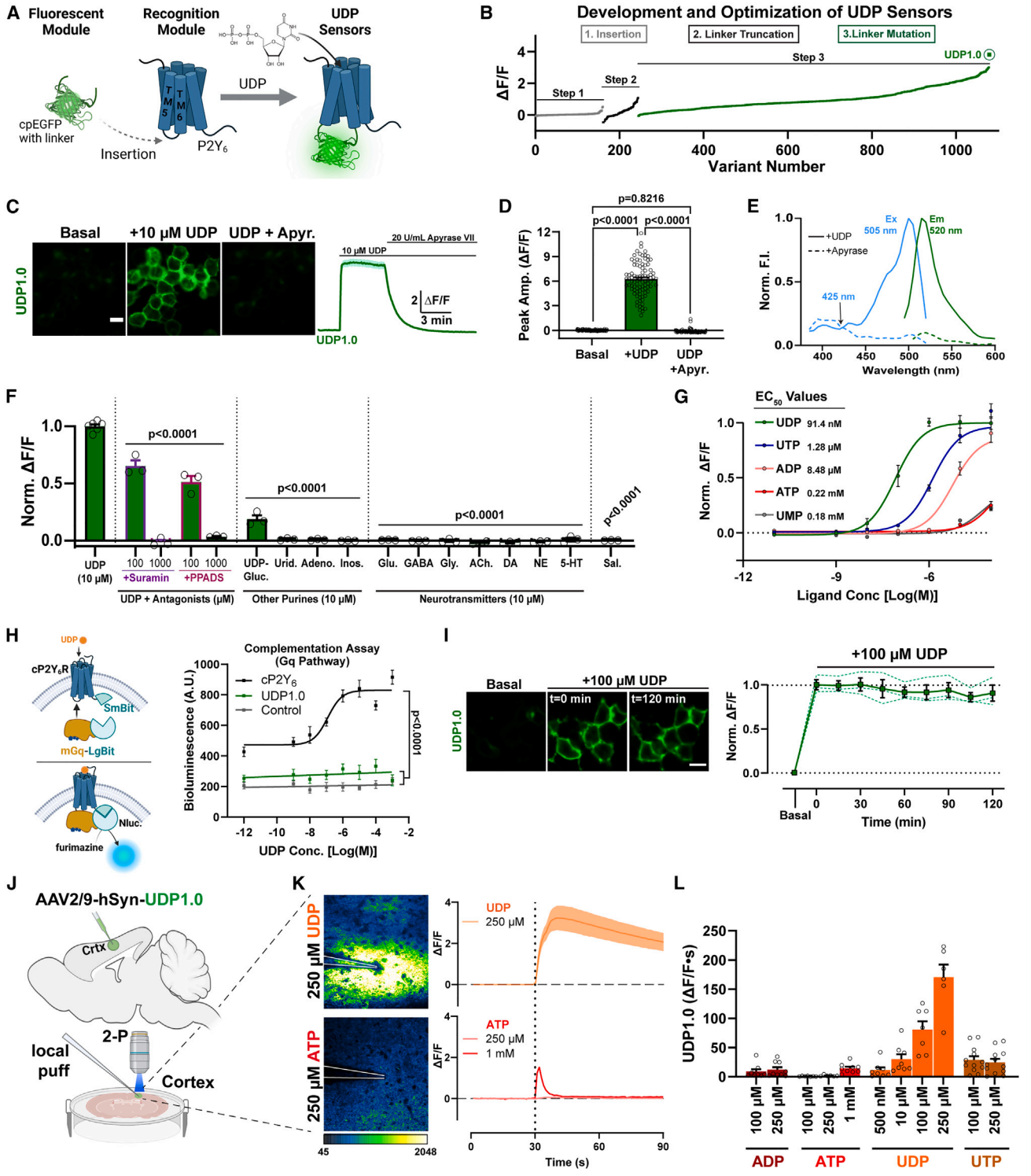

Figure 2. Development of a fluorescent sensor for *in vivo* imaging of extracellular UDP

(A) Engineering the UDP biosensor.

(B) Optimization of the UDP sensor through a three-step process, including insertion site optimization, linker truncation, and linker sequence optimization, yielding the UDP1.0 variant (see Figures S1A and S1B).

(C) Images and corresponding ΔF/F trace of UDP1.0 fluorescence under basal conditions, following 10 μM UDP application, and following 20 U/mL apyrase grade VII (apyr.) treatment (HEK293T cells). Scale bar, 20 μm.

(legend continued on next page)

Please cite this article in press as: Umpierre et al., Microglial P2Y$_6$ calcium signaling promotes phagocytosis and shapes neuroimmune responses in epileptogenesis, Neuron (2024), https://doi.org/10.1016/j.neuron.2024.03.017

Enhanced UDP release occurs following status epilepticus

To understand endogenous UDP dynamics in the mouse brain, we performed longitudinal two-photon imaging in the somatosensory cortex following AAV2/9-hSyn-UDP1.0 transfection (awake mouse chronic window preparations; Figures 3A–3G). At baseline, *in vivo* UDP release events are rare (0.7 events/30 min; 620 × 620 μm field of view). However, soon after KA-SE, UDP release events increase to 16.8 ± 3.4 events/30 min (Figure 3D; Video S1) and remain elevated for the first 72 h of epileptogenesis. During early epileptogenesis, UDP release events are prolonged (Figures 3D and 3E), enhancing their average signal area (Figure 3D). UDP release events can be categorized by two distinctive ΔF/F kinetic signatures. Type 1 events have a unique "sharp peak" created by near-instantaneous rise kinetics followed by two-component exponential decay (Figures 3B and S1H). These events only occur during acute excitotoxicity (40% ± 3.3% of events 2–6 h post-SE) and can be modeled *ex vivo* by highly transient UDP application (Figures 3C and S1G). Type 2 events have slower (multi-second) rise kinetics followed by single-order exponential decay kinetics (Figures 3B and S1H). Type 2 release kinetics predominate across all periods and can be modeled by prolonged UDP application (Figure 3C). Overall, *in vivo* biosensor imaging indicates that microglia can be exposed to a far greater physical area of UDP release (Figure 3F) and a stronger UDP signal (Figure 3G) during early epileptogenesis.

We additionally surveyed UDP release dynamics in the hippocampus using acute brain slice preparations (Figure 3H). UDP release dynamics are reasonably similar between *ex vivo* and *in vivo* preparations (see STAR Methods; Figures S2A–S2C). Similar to the cortex, UDP release events are infrequent in naive hippocampal slices (2.29 ± 0.38 events/ 30 min). However, UDP release events are increased 3- to 9-fold in frequency 3–7 days after KA-SE excitotoxicity (D3: 28.33 ± 2.93; D7: 11.36 ± 0.83 events/ 30 min; Figure 3I), with an ∼160% increase in average physical size (306 ± 29 μm^2 naive vs. 497 ± 87 μm^2 D7, p = 0.0194; Welch's t test). UDP release event area and frequency remain above baseline levels at least 10 days after KA-SE in the CA3 region (Figure 3I). Therefore, microglia should be exposed greater levels of extracellular UDP in hippocampus during epileptogenesis.

Finally, to determine whether UDP release is a conserved response to excitotoxicity, we exposed acute brain slices to 0 Mg^{2+} artificial cerebrospinal fluid (aCSF) conditions, which can result in epileptiform burst activity within minutes.[27] Similar to KA-SE, transitioning brain slices from normal aCSF to 0 Mg^{2+} conditions rapidly increases extracellular UDP release (Figures S3A and S3B; Video S2). During 0 Mg^{2+} aCSF conditions, type 1 (sharp peak) UDP release events emerge (Figure S3B) and significantly increase the maximum amplitude and signal area of UDP release compared to normal aCSF (Figure S3C). Overall, 0 Mg^{2+} excitotoxic conditions double UDP release frequency across cortical layers, from an average of 6 events to 14.25 events (Figures S3D and S3E).

Microglial calcium elevations during epileptogenesis are P2Y$_6$ dependent

Enhancements in UDP release and P2Y$_6$ sensitivity may significantly contribute to microglial calcium signaling during epileptogenesis. To test our hypothesis, P2Y$_6$ knockout (KO: *P2ry6*$^{-/-}$) and WT (*P2ry6*$^{+/+}$) lines were bred to microglial calcium reporter mice (Cx3Cr1$^{CreER\text{-}IRES\text{-}eYFP}$; R26$^{LSL\text{-}CAG\text{-}GCaMP6s}$). In RNA-based assays, *P2ry6*$^{-/-}$ microglia have a confirmed loss/attenuation of *P2ry6* transcript without changes in other P2X or P2Y gene family members (Figures S4A and S4B). In acute slice preparations, *P2ry6*$^{-/-}$ microglia have reduced calcium responses to UDP and a P2Y$_6$R agonist (MRS-2693; Figures S4C–S4H). *P2ry6*$^{-/-}$ microglia also have attenuated process chemotaxis toward UDP (Figure S4J), while ATP calcium responses (Student's t test, p = 0.9999) and chemotaxis are unchanged (Figure S4I). UDP release dynamics in tissue are also similar (Figure S3D). These results verify that *P2ry6*$^{-/-}$ microglia have attenuated UDP calcium and motility responses without noted effects on UDP release or ATP responses.

Using *in vivo* two-photon imaging (Figure 4A), we first discovered that P2Y$_6$ deficiency has little impact on spontaneous microglial calcium signaling (Figures 4B–4D) or process motility in a naive state (Figures 4I and 4J). On the other hand, there are substantial differences in microglial calcium signaling between genotypes during epileptogenesis. Over the first week of epileptogenesis, approximately half of all *P2ry6*$^{+/+}$ microglial processes transition from an inactive to a highly active calcium signaling state (Figures 4B–4D). In *P2ry6*$^{-/-}$ microglia, the transition to high-level calcium signaling is strongly attenuated, with the majority of processes retaining low-to-absent calcium signaling profiles during early epileptogenesis (Figures 4B–4D; Video S3). We would therefore conclude that microglia without P2Y$_6$ expression have significantly reduced calcium signaling in the first 2 weeks of epileptogenesis (Figure 4E), which is not likely due to differences in KA sensitivity or differences in initial seizure severity (Figure 4F; see STAR Methods).

(D) Summary of peak UDP1.0 ΔF/F amplitudes. One-way ANOVA with Tukey's post hoc test (90 total cellular ROIs).
(E) One-photon excitation (Ex) and emission (Em) spectra for UDP1.0 in the presence of 10 μM UDP (solid lines) or 5 U/mL apyr. (dashed lines).
(F) Comparison of UDP responses in the presence of non-selective P2Y receptor antagonists or other purine agonists, neurotransmitters, and saline. Peak ΔF/F responses were normalized to UDP. One-way ANOVA with post hoc UDP comparison.
(G) UDP1.0 fluorescent response curves for purinergic ligands and associated EC_{50} values (see STAR Methods for fitting; 3–6 wells and 300–500 cells/well).
(H) Left: schematic of the complementation assay. Right: total luminescence emitted by cells co-transfected with LgBit-mGq alone (control), LgBit-mGq with cP2Y$_6$-SmBit, or LgBit-mGq with UDP1.0-SmBit. One-way ANOVA with Tukey's post hoc test (3 wells/group).
(I) UDP1.0 fluorescence in HEK cells with 2-h UDP incubation (100 μM). One-way ANOVA with post hoc comparison to UDP incubation start: p ≥ 0.8934. Scale bar, 10 μm. Solid line, mean ± SEM; dashed line, one of three wells containing 300–500 cells.
(J) Schematic illustration of the UDP1.0 acute brain slice characterization experiments.
(K) UDP1.0 fluorescent responses to UDP or ATP (left) and example traces (right: overall ΔF/F mean ± SEM response from 4–6 trials).
(L) Summary of UDP1.0 signal response areas for different purinergic signals in brain slice (mean ± SEM from 4–8 independent trials and slices from n = 3–4 mice).

Please cite this article in press as: Umpierre et al., Microglial P2Y$_6$ calcium signaling promotes phagocytosis and shapes neuroimmune responses in epileptogenesis, Neuron (2024), https://doi.org/10.1016/j.neuron.2024.03.017

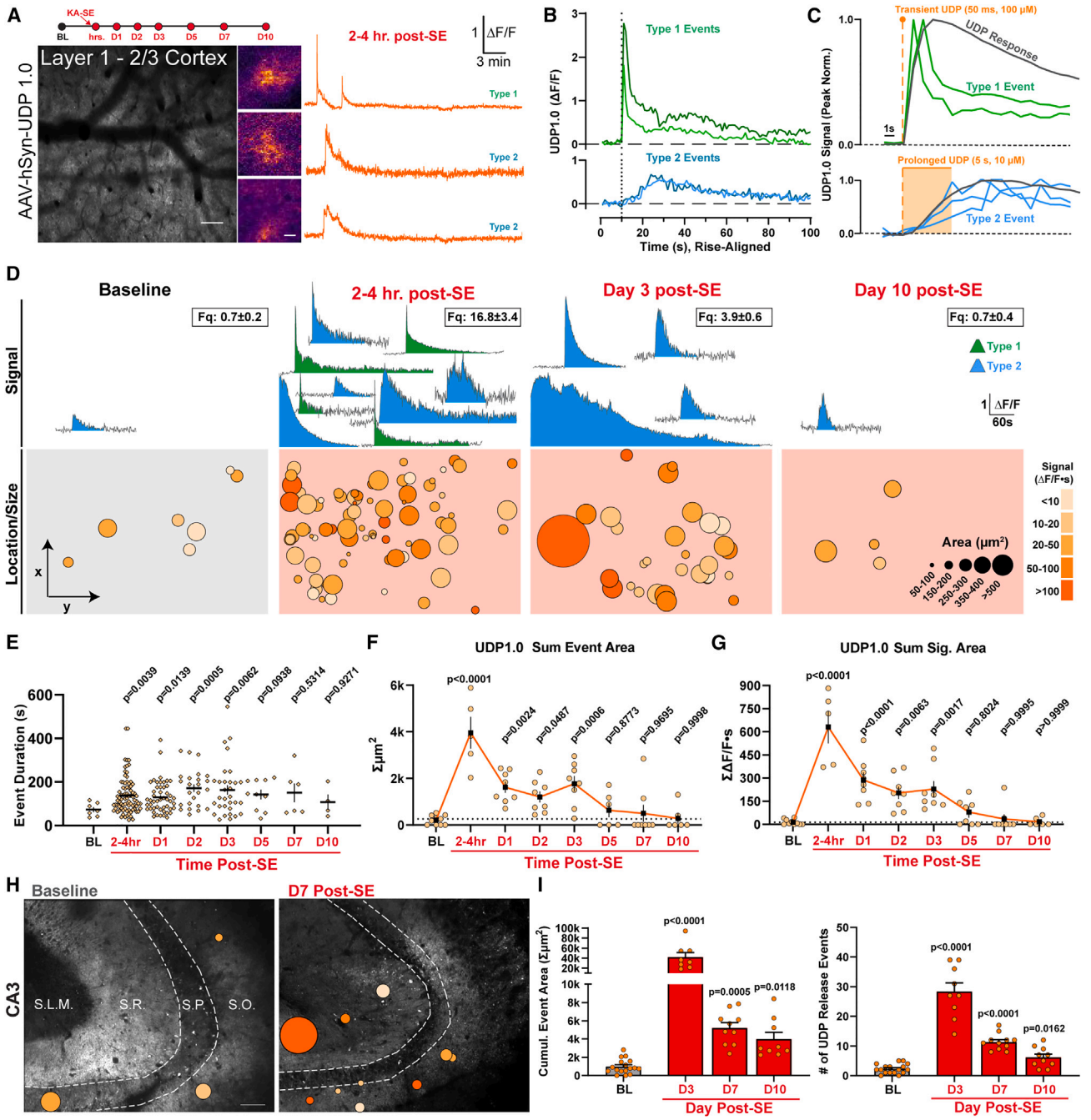

Figure 3. Enhanced UDP release occurs following status epilepticus

(A) *In vivo* two-photon study timeline and image of UDP1.0 expression in the somatosensory cortex. Scale bar, 100 μm. Example UDP event fluorescence and corresponding ΔF/F traces. Scale bar, 20 μm.

(B) Examples of type 1 sharp-peak and type 2 UDP events (ΔF/F traces aligned to rise start time).

(C) Modeling type 1 and type 2 rise kinetics (peak normalized) with transient or prolonged UDP application *ex vivo* (gray trace).

(D) Example UDP sensor signals (top, ΔF/F) and sensor event size/location under the cranial window (bottom). The number of ΔF/F signals displayed (top) conveys frequency (box, mean ± SEM events per 30 min recording). Event size/location displays all events aggregated across a longitudinal cohort of n = 3–5.

(E) Duration of UDP release events (dot, a single event).

(F) The cumulative area covered by UDP sensor events over a 30 min period (dot, one imaging region).

(G) The cumulative UDP ΔF/F•s signal recorded over a 30 min period (dot, one imaging region).

(H) Overlay of UDP sensor events *ex vivo* in the CA3 region of hippocampus. Scale bar, 70 μm. Event scale as in (D).

(legend continued on next page)

Please cite this article in press as: Umpierre et al., Microglial $P2Y_6$ calcium signaling promotes phagocytosis and shapes neuroimmune responses in epileptogenesis, Neuron (2024), https://doi.org/10.1016/j.neuron.2024.03.017

Similar to the cortex, $P2Y_6$ deficiency also reduces microglial calcium signaling in the hippocampus. As an important comparative control, cortical microglia display reasonably similar patterns of calcium activity in both *ex vivo* and *in vivo* preparations (Figures S2D–S2H). At baseline, *P2ry6*$^{+/+}$ and *P2ry6*$^{-/-}$ microglia have similarly rare spontaneous calcium activity in the hippocampus (Figures 4G and 4H). However, *P2ry6*$^{+/+}$ microglia display clear enhancements in spontaneous calcium activity 1–10 days after KA-SE in hippocampus compared to *P2ry6*$^{-/-}$ microglia (CA1 and CA3 regions: Figures 4G and 4H). Taken together, enhanced spontaneous microglial calcium activity can be a widespread feature of epileptogenesis and is primarily related to $P2Y_6$ signaling in microglia.

$P2Y_6$ signaling is associated with lysosome biogenesis and can facilitate neuronal engulfment

The function of $P2Y_6$ signaling in epileptogenesis is not definitively known. However, $P2Y_6$ activation can promote phagocytosis in both sterile[24,28–31] and infection-based contexts.[24] In *P2ry6*$^{+/+}$ tissue, we observe an expansion in CD68$^+$ phagolysosome area over the first 3–7 days following KA-SE (Figures S5A and S5B), which is most pronounced in limbic regions known to have dead or dying neurons[8,9] (hippocampus, amygdala, and thalamus; Figures 5A and 5B). At the cellular level, the majority of CD68 expression is attributable to microglia through TMEM119 co-staining (Figures 5C and 5D) or flow cytometry (Figure 5E). In KO tissue, loss of the $P2Y_6$ pathway substantially limits CD68 expansion across limbic brain regions during epileptogenesis (Figures 5A and 5B). Genotype-dependent differences in lysosome expansion are also observed using the lysosome marker LAMP1 (Figures S5H–S5J). As an important control, baseline levels of CD68 and LAMP1 expression are equivalently low in the naive state for both genotypes (Figures S5B and S5I). Therein, $P2Y_6$ deficiency can limit the biogenesis or expansion of lysosome area in microglia during early epileptogenesis. On the other hand, $P2Y_6$ KO does not influence microglial morphology during epileptogenesis, as the progression and extent of ameboid transition is similar between genotypes in hippocampus (Figures 5F and 5G). Correlations between initial seizure severity (see STAR Methods) and microglial ameboid transition (Figure 5H, top) or lysosome area (Figure 5H, bottom) suggest that $P2Y_6$ signaling can influence microglial lysosome biogenesis in epileptogenesis without observed alterations in ameboid state transition.

In the CA3 region, phagolysosome expansion is most substantial in the pyramidal cell layer, (*stratum pyramidale* [SP]), which contains the soma of principal neurons (Figures S5A and S5C). We evaluated whether microglia could be engaged in the phagocytosis of neuronal somata (Video S4). CD68-NeuN interactions were qualified as no/minimal coverage, moderate coverage, or full engulfment (see Figure 5I and STAR Methods). In day 7 tissue, approximately 40% of WT CA3 neurons had a moderate level of contact by CD68$^+$ cells (54 ± 7 pyramidal neurons per 212 × 212 × 20 μm volume), and approximately 10 neurons per imaging volume reached full engulfment criteria (6.3%, or 95 of 1,501 neurons in day 7 tissue; Figure 5J). In *P2ry6*$^{-/-}$ mice, virtually no CA3 neuron reached full engulfment criteria (0.13%, or 2 of 1,529 neurons; Figure 5J). Notably, *P2ry6*$^{-/-}$ IBA1 cells appear to have a deficit in their ability to either migrate into the pyramidal layer or expand therein (Figures S5D and S5E), resulting in reduced IBA1-NeuN interactions and CD68-NeuN interactions (Figures S5F and S5G). TMEM119 co-staining demonstrates that microglia perform the majority of neuronal engulfment in *P2ry6*$^{+/+}$ tissue rather than outside macrophage populations (Figure 5K). Collectively, these results suggest that *P2ry6*$^{-/-}$ microglia have an impaired ability to contact and phagocytose neuronal somata in epileptogenesis.

Attenuating calcium signaling through CalEx phenocopies lysosome impairments in microglia

To identify whether calcium activity is particularly important for the phagocytic process, we overexpressed a calcium extruder protein (ATP2B2, or "CalEx") selectively in microglia (TMEM119$^{2A\text{-}CreERT2}$ × R26$^{LSL\text{-}CAG\text{-}ATP2B2\text{-}mCherry}$). ATP2B2 is a transmembrane protein that facilitates the rapid removal of calcium from the cytosol, reducing calcium signaling time[32,33] (Figure 6A). We confirmed that CalEx recombination occurs selectively in microglia and in a Cre-dependent manner (mCherry tag; Figures 6B and 6C). However, recombination was not always robust across brain regions (Figure 6C), limiting evaluations at the systems level. To validate CalEx function, we used an improved viral delivery system to target GCaMP6f to CA1 microglia[34] (rAAV-SFFV-DIO-GCaMP6f-WPRE-hGH) and performed calcium imaging *ex vivo* (Figure 6D). In GCaMP6f-expressing control microglia (TMEM119$^{2A\text{-}CreERT2}$; R26$^{wt/wt}$), focal UDP application leads to an expected, long-lasting calcium response (42.0 ± 1.6 s; Figures 6E–6G). However, in microglia with confirmed mCherry-CalEx expression (Figure 6E), UDP application results in a significantly shortened calcium response (16.8 ± 1.3 s; Figures 6F and 6G), demonstrating that CalEx can reduce the time course of UDP-driven microglial calcium elevations.

In the process of characterizing CalEx function, we observed an interesting patchwork of CD68 expression in CA1 S.R. one week after KA-SE (Figure 6H). Upon further investigation, we found that IBA1 cells with CalEx expression (mCherry$^+$) had significantly reduced CD68 levels compared to adjacent mCherry$^-$ IBA1 cells of the same tissue (Figure 6I). In mCherry$^+$ microglia, CD68 staining was smaller in size and occupied less IBA1 cell area (Figure 6J), suggesting that calcium extrusion may also prevent lysosome maturation and expansion in hippocampal microglia. Interestingly, adjacent mCherry$^+$ and mCherry$^-$ microglia do not differ in their IBA1-based Sholl morphologies despite differences in CD68 expression (Figure 6K). CalEx expression additionally influences the extent of

(I) Quantification of cumulative UDP release area and UDP release event frequency per 30 min. One-way ANOVA with Dunnett's post hoc comparison to baseline (dot, one CA3 region surveyed per slice; 2–3 slices and n = 4 mice per time point).
(D–G) Longitudinal study of 2 non-overlapping regions from n = 3–5 mice. (E–G) One-way ANOVA with Fisher's post hoc testing vs. baseline for statistical comparison.
Bar or line graphs represent the mean ± SEM.

Please cite this article in press as: Umpierre et al., Microglial P2Y$_6$ calcium signaling promotes phagocytosis and shapes neuroimmune responses in epileptogenesis, Neuron (2024), https://doi.org/10.1016/j.neuron.2024.03.017

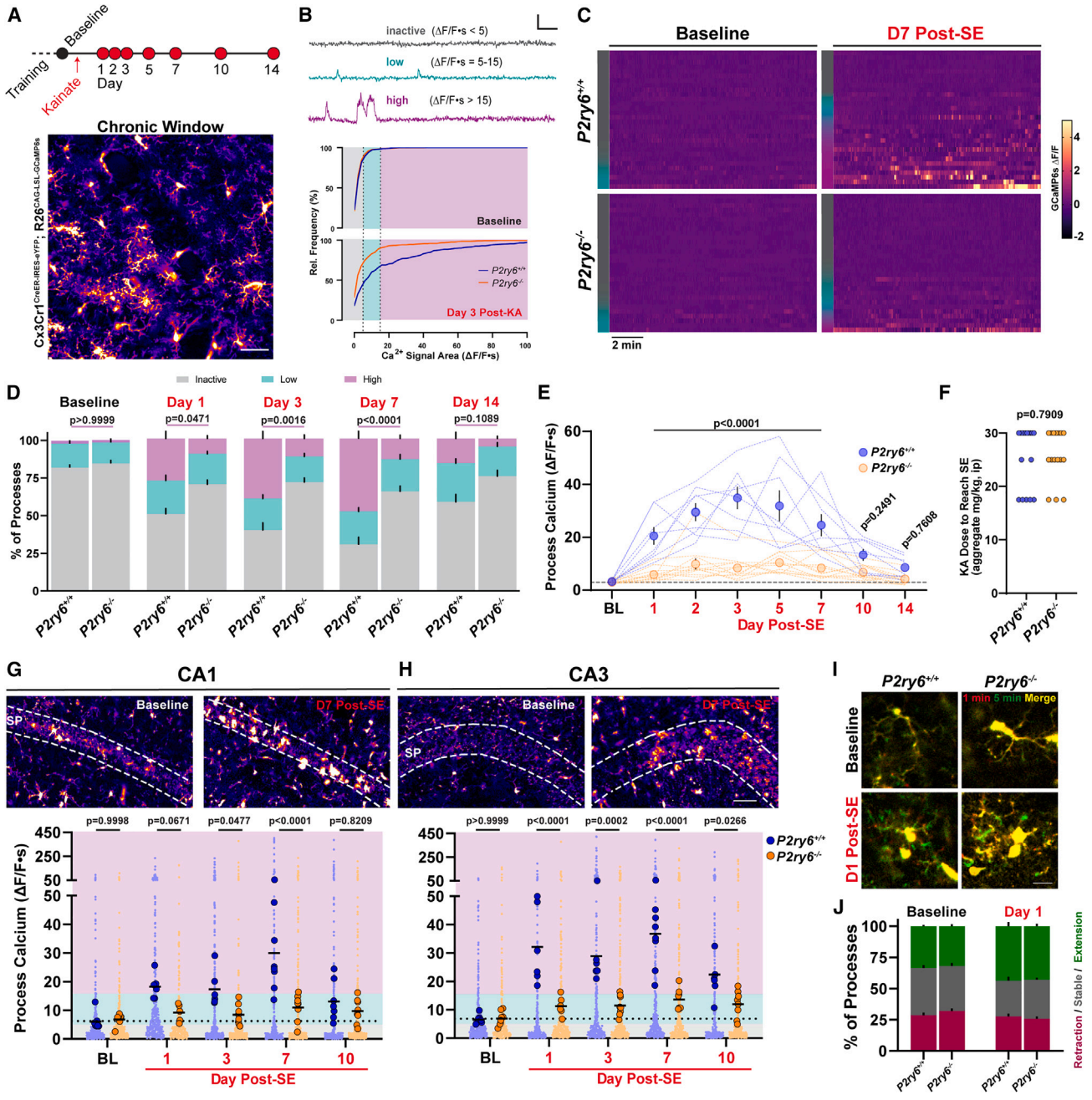

Figure 4. Microglial calcium elevations during epileptogenesis are P2Y$_6$ dependent

(A) Experimental timeline and example field of view for *in vivo*, longitudinal calcium imaging of microglia. Scale bar, 40 μm.

(B) Top: examples of inactive, low-level, and high-level microglial process calcium signaling. Scale bar, 1-fold ΔF/F and 60 s. Bottom: microglial process calcium activity distributions (ΔF/F•s) at baseline and 3 days after KA-SE.

(C) Heatmaps of microglial GCaMP6s calcium activity (ΔF/F) by genotype and time period (30 process ROIs chosen to match inactive/low/high activity distributions, left color bar).

(D) Percentage of total microglia process ROIs exhibiting no, low, or high activity between genotypes. Two-way ANOVA with Sidak's post hoc test between activity levels (p value compares high-level activity).

(E) Overall calcium activity across 2 weeks of epileptogenesis. Two-way ANOVA with Sidak's post hoc test (dotted lines represent a longitudinal imaging region; dots represent group mean ± SEM).

(F) Comparison of the aggregate KA dose needed to reach SE between genotypes. Mann-Whitney test (n = 17 *P2ry6*$^{+/+}$ mice and n = 16 *P2ry6*$^{-/-}$ across 3 independent cohorts).

(legend continued on next page)

phagocytic microglial interactions with hippocampal neurons (Figure 6L), similar to P2Y$_6$ KO evaluations (Figures 5I and 5J). In particular, CalEx/mCherry$^+$ cells are less likely to fully engulf hippocampal neurons than neighboring mCherry$^-$ IBA1 cells (Figure 6M) despite their similar prevalence in the pyramidal band (Figure 6N). Thus, CalEx studies further support the importance of calcium signaling for microglial lysosome regulation and phagocytic interactions without clear impact on morphology.

Enhanced pro-inflammatory signaling is coordinated with phagocytosis in *P2ry6*$^{+/+}$ microglia

We additionally turned to bulk RNA sequencing (RNA-seq) analyses to potentially uncover unique roles for the P2Y$_6$ pathway in regulating microglial function. Microglia were isolated from whole brains of *P2ry6*$^{+/+}$ and *P2ry6*$^{-/-}$ mice 3 days after KA-SE (Figure 7A). In comparing transcriptomes between genotypes soon after KA-SE, a highly specific profile emerged, with most differentially expressed genes (DEGs) mapping on to immune-related function (Figures 7B and 7C). In particular, P2Y$_6$ function may be closely tied to *Trim* gene regulation. Tripartite motif-containing (TRIM) proteins represent a superfamily of E3 ubiquitin ligases that regulate multiple inflammatory pathways, including type I interferon (IFN) and NF-κB transcription.[35,36] Notably, top upregulated genes in WT mice—*Trim12*, *Trim 30b*, *Trim30d*, and *Trim34a*—are all positive regulators of NF-κB transcription, while top downregulated genes—*Mturn* and *Trim21*—are negative regulators of NF-κB transcription.[35,37] From these insights, we further evaluated P2Y$_6$ signaling through an immunological lens by assessing its impact on NF-κB-related inflammation.

We used high-parameter flow cytometry to analyze microglia 5 days after KA-SE in hippocampus and cortex (Figure 7D). As a broad indication of activation state, *P2ry6*$^{+/+}$ microglia have a reduced intensity of the homeostatic marker P2Y$_{12}$ and an increased intensity of Cx3Cr1[38] when compared to *P2ry6*$^{-/-}$ microglia in hippocampus (Figure 7E). Activation of the NF-κB transcriptional pathway can result in the production of multiple pro-inflammatory cytokines, including interleukin 1 (IL-1), IL-6, and tumor necrosis factor alpha (TNF-α). In uniform manifold approximation and projection (UMAP) plots, we observe that a subpopulation of *P2ry6*$^{+/+}$ microglia has enriched TNF-α and Pro IL-1β expression (Figure 7F), increasing the overall frequency of TNF-α and Pro IL-1β expression in the hippocampus (vs. naive or *P2ry6*$^{-/-}$ microglia; Figure 7G). Genotype-dependent cytokine differences appear to be relatively specific to the NF-κB pathway, as no differences were observed in type II IFN levels, the cGAS-STING pathway, or other interleukins studied (Figures 7H and 7I). In addition, we did not observe differences in the frequency of microglial surface marker expression between genotypes for CD11c, CD25, CD122, CD126, MERTK, and MHCII (data not shown). Taken together, transcriptomic and flow cytometry findings support a potential role for P2Y$_6$ signaling in modulating NF-κB-related inflammation.

We additionally evaluated differences in phagocytic populations between *P2ry6*$^{+/+}$ and *P2ry6*$^{-/-}$ microglia using flow cytometry. Consistent with immunofluorescence staining, *P2ry6*$^{+/+}$ microglia more frequently and more robustly express CD68 in hippocampus (Figures 7F and 7G). After gating for microglial populations (Figures S7A and S7B), we found that *P2ry6*$^{+/+}$ hippocampal microglia are more likely to have a co-detected NeuN signal than *P2ry6*$^{-/-}$ microglia, which could represent neuronal phagocytosis in early epileptogenesis (Figure 7J) given immunofluorescent findings (Figures 5 and S5). With flow cytometry, we identified and analyzed unique subpopulations of microglia based on CD68 levels, including low CD68 expression, high CD68 expression, and high CD68 expression in combination with high side scatter (SSC)—an indication of greater cell density (Figure 7K). In WT microglia, associated NeuN signal intensity progressively increases between subpopulations, potentially suggesting greater levels of neuronal phagocytosis (Figure 7L). Each population is also increasingly more activated (based on Cx3Cr1 intensity) and inflammatory (based on TNF-α, IL-2, and Pro IL-1β expression; Figure 7L). Taken together, these observations suggest that pro-phagocytotic microglia (CD68^{High} and CD68^{High};SSC^{High}) are more likely to be pro-inflammatory (also seen in UMAP visualization: Figure 7F). Microglia with coincident phagocytic and inflammatory profiles may have implications for neurodegeneration[39–41]: there are strong associations between microglial IL-1β and NeuN levels (flow cytometry; Figure 7N), while IBA1 cells with the highest IL-1β expression often localize to the pyramidal band (immunofluorescence; Figure 7M). Most importantly, highly phagocytic (CD68^{High};SSC^{High}), pro-inflammatory microglia are more prominent in the *P2ry6*$^{+/+}$ hippocampus, while less inflammatory CD68^{Low} microglia are more prominent in *P2ry6*$^{-/-}$ hippocampus (Figures 7F and 7O).

Loss of P2Y$_6$ expression reduces myeloid cell infiltration

By evaluating other immune cell populations in the *P2ry6*$^{+/+}$ and *P2ry6*$^{-/-}$ brain, we discovered that the *P2ry6*$^{+/+}$ hippocampus also experiences more CD45^{High} immune cell infiltration (Figure S6C). Based on cell-type markers, infiltrating myeloid cells are particularly more abundant in the *P2ry6*$^{+/+}$ hippocampus 5 days after KA-SE (Figure S6D). T and natural killer (NK) cell levels are similar between genotypes (Figure S6D). Infiltrating myeloid cells are highly pro-inflammatory, having greater Pro IL-1β expression than even activated microglia (Figure S6E).

There are multiple potential mechanisms for P2Y$_6$ deficiency to influence myeloid cell infiltration. Myeloid cells are known to express the P2Y$_6$ receptor, and we can detect *P2ry6* mRNA associated with non-microglial (*Tmem119*$^-$) immune cells (*Ptprc*$^+$, the CD45 protein; Figures S7A and S7B). In surveying multiple brain

(G) Top: 2P images of microglia in acute brain slice CA1. Bottom: spontaneous calcium activity in CA1 microglia across epileptogenesis. Two-way ANOVA with Sidak's post hoc test of slice averages (small dot, one process ROI; large circle, slice average; survey of 2 slices/mouse and n = 3–4 mice/group).
(H) As in (G), for microglial processes of the CA3 region. Scale bar, 50 μm.
(I) *In vivo* average intensity images of microglia to indicate process motility. Scale bar, 15 μm.
(J) Percentage of processes that extend outward, remain stable, or retract during *in vivo* imaging. Two-way ANOVA with Sidak's post hoc test: no significant motility differences between genotypes (p = 0.5505–0.9965 by motility type).
Bars represent the mean ± SEM. *In vivo* (A–E): n = 4 *P2ry6*$^{+/+}$mice, n = 6 *P2ry6*$^{-/-}$ mice with 2 non-overlapping regions surveyed per mouse.

Please cite this article in press as: Umpierre et al., Microglial P2Y$_6$ calcium signaling promotes phagocytosis and shapes neuroimmune responses in epileptogenesis, Neuron (2024), https://doi.org/10.1016/j.neuron.2024.03.017

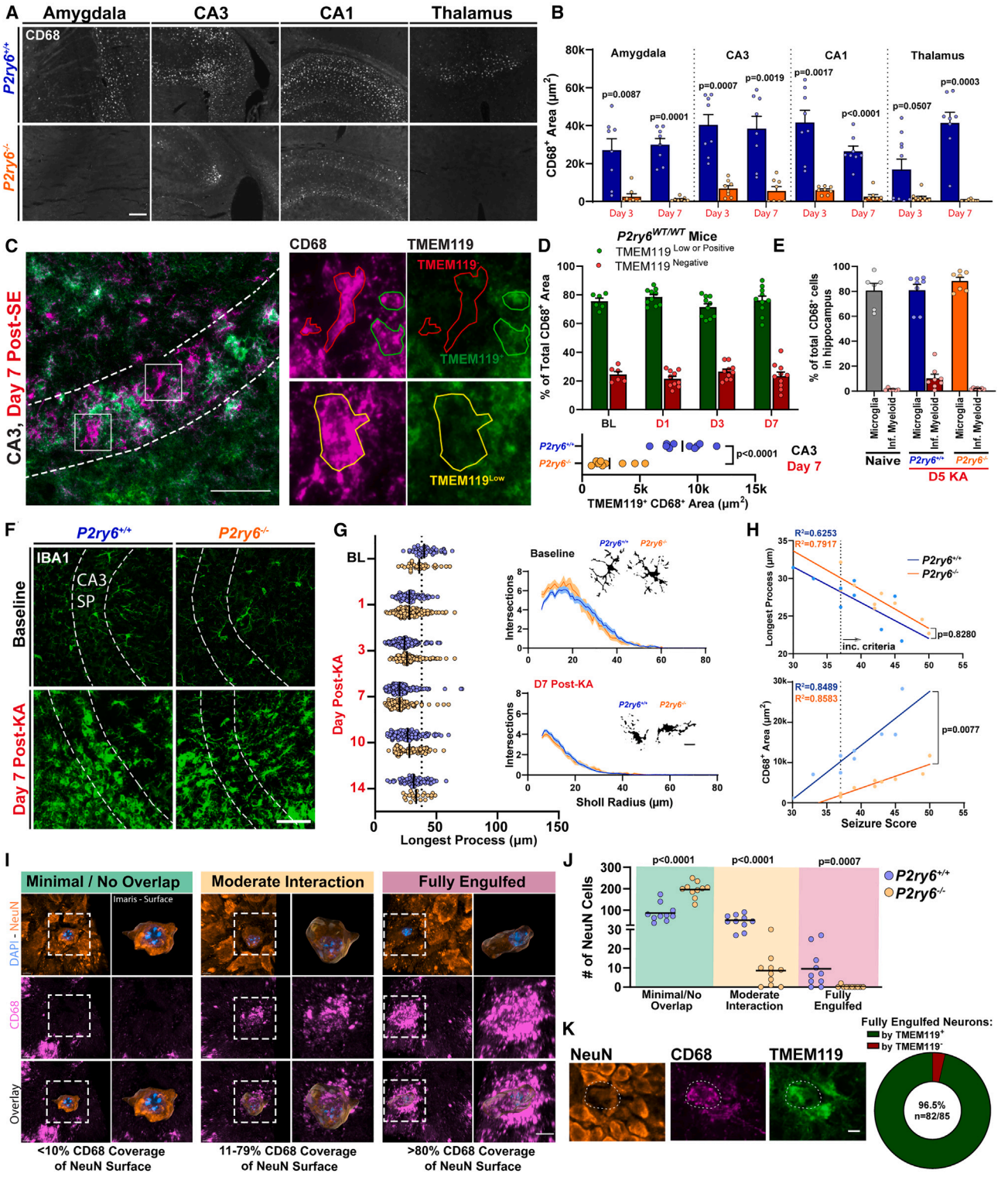

Figure 5. P2Y$_6$ activation regulates lysosome biogenesis and facilitates neuronal soma engulfment

(A) CD68 expression across limbic regions 3 days after KA-SE. Scale bar, 100 μm.

(B) Quantification of CD68 area. One-way ANOVA with Dunnett's post hoc test by region (dots, one region; two regions from n = 4–5 mice/group).

(C) CD68 expression in CA3 and its localization to regions that are TMEM119$^+$, TMEM119^{Low}, or TMEM119$^-$. Scale bar, 50 μm.

(legend continued on next page)

Please cite this article in press as: Umpierre et al., Microglial P2Y$_6$ calcium signaling promotes phagocytosis and shapes neuroimmune responses in epileptogenesis, Neuron (2024), https://doi.org/10.1016/j.neuron.2024.03.017

regions 3 and 7 days after KA-SE, non-microglial immune cells with *Ccr2* transcription (*Tmem119*$^-$;*Ccr2*$^+$;*Ptprc*$^+$) have similarly high levels of *P2ry6* puncta as microglia (Figure S7C). However, it is not clear whether UDP could *directly* promote the recruitment of outside myeloid (or immune) cells through their specific P2Y$_6$ receptor activation. Indirectly, UDP engagement of P2Y$_6$ signaling can enhance local chemokine production to increase recruitment (e.g., increased CXCL8 production in the intestines[42]). We evaluated whether UDP could directly recruit isolated macrophage populations in a transwell assay (Figures S7D–S7F). Intriguingly, both UDP (1 μM and 10 μM) and the high-affinity P2Y$_6$ agonist MRS-2693 (10 μM) could induce macrophage migration/invasion across the transwell mesh (8 μm pore) at levels significantly above the negative control (serum-free media). UDP- and MRS-based migration was similar to positive control levels (10% fetal bovine serum [FBS]; Figures S7G and S7H) but not as robust as CCL2-based migration/invasion (Figures S7G and S7H). Therein, UDP could serve as a recruitment signal to peripheral myeloid cells in *in vitro* studies.

P2Y$_6$ KO mice have improved CA3 neuronal survival and enhanced cognitive task performance

Over time, there are multiple indications of poorer neuronal health in *P2ry6*$^{+/+}$ hippocampus. In flow cytometry, neurons in the *P2ry6*$^{+/+}$ hippocampus are twice as likely to express TNF-α 5 days after seizures, while astrocyte TNF-α expression is similar between genotypes (Figures S6F and S6G). Histological evaluation (Fluoro-Jade C [FJC]) suggests that neuron death or damage is initially similar between genotypes but begins to reduce in KO tissue while remaining elevated in WT tissue (day 7 in amygdala, CA3, and CA1; Figures S8A and S8B). Interestingly, in CalEx-expressing tissue, we also observe reduced FJC levels in multiple hippocampal regions, including the CA1 and hilus (vs. tamoxifen-restricted controls on day 7; Figure S8B). As a proxy for initial seizure severity,[43,44] both *P2ry6*$^{+/+}$ and *P2ry6*$^{-/-}$ tissue had similar levels of immediate-early gene expression 1 day after KA-SE (c-Fos; Figures S8C and S8D).

P2Y$_6$ deficiency is associated with greater CA3 neuron survival in early epileptogenesis. In *P2ry6*$^{+/+}$ mice, progressive loss of CA3 neurons occurs over the first week of epileptogenesis, resulting in a 40% reduction in NeuN density (Figures 8A–8C). However, in *P2ry6*$^{-/-}$ mice, NeuN loss does not appear to progress beyond 24 h after KA-SE, with a consistent observation that only 15% of CA3 neurons are lost across later histological time points (Figure 8C). These findings are also corroborated by cresyl violet staining in day 10 and day 14 tissue (Figures S8E and S8F).

We next assessed whether differences in observed CA3 neuron loss had an impact on cognition using the novel object recognition (NOR) task, which relies upon CA3 neuron function.[45,46] NOR performance was assessed in the same cohort of *P2ry6*$^{+/+}$ and *P2ry6*$^{-/-}$ mice at baseline (naive state) and 1 week following KA-SE (Figure 8D). In the naive test, mice first explored two identical objects in the familiarization phase, with neither genotype displaying an object preference (50:50 ratio; Figure 8F). In the novel phase (30 min delay), mice from both genotypes preferentially explored the novel object, resulting in a discrimination index score that was both above chance (0.50; one-sample t test) and above their discrimination scores in the familiar phase (Figures 8E and 8F; two-way ANOVA with Sidak's post hoc test). One week after KA-SE (10 days after the prior test), we re-tested NOR performance using different object sets. Familiarization phase performance occurred at the expected 50:50 ratio for both genotypes (Figure 8H). However, in the novel phase, *P2ry6*$^{+/+}$ mice failed to explore the novel object at levels that were significantly distinguishable from either chance (one-sample t test) or their performance in the familiarization phase (Figures 8G and 8H; two-way ANOVA with Sidak's post hoc test). On the other hand, *P2ry6*$^{-/-}$ mice could still distinguish a novel object from a familiar object 1 week after KA-SE, evidenced by both above-chance and above-familiar phase task performance (Figures 8G and 8H). Using ezTrack,[47] we found that animal movement was similar between genotypes for all test periods and phases (Figure 8I), indicating that animal mobility was not a confounding factor. NOR testing suggests that mice lacking the P2Y$_6$ pathway better maintain cognitive task performance in early epileptogenesis.

DISCUSSION

The cell-type specificity of the P2Y$_6$ pathway and consideration of key outcomes

Most studies have focused on the role of ATP in promoting microglial calcium signaling in culture[48] and *in vivo*.[5] Our findings suggest that UDP can also elicit large calcium transients in microglia. General KO of the P2Y$_6$ receptor attenuates microglial calcium activity and neuroimmune responses following KA-SE. When evaluating key outcomes, one must consider (1) whether the methods used can sufficiently distinguish between microglia

(D) Top: CD68 immunofluorescent area in CA3 colocalized to either TMEM119$^{Low\ or\ +}$ regions or TMEM119$^-$ regions. Bottom: quantification of TMEM119-localized CD68 area between genotypes. Student's t test (dot, one CA3 region from n = 3–5 WT mice/group).
(E) Percentage of hippocampal CD68$^+$ cells that are microglia or infiltrating myeloid cells in flow cytometry (see Figure S7 for gating).
(F) IBA1 staining in the CA3 region for Sholl analyses. Scale bar, 40 μm.
(G) Left: CA3 microglia longest process analyses. Two-way ANOVA effect of genotype: $F_{(1,\ 1094)} = 0.5979$, p = 0.4395 (dot, one cell). Right: Sholl plots with representative cell morphologies. Scale bar, 5 μm. n = 3–5 mice/group and 10–40 cells/mouse.
(H) Correlations between initial seizure severity and either CA3 microglial process length (top) or total CD68 area (bottom). Simple linear regression (dot, one mouse from day 3 and day 7 time points).
(I) Histological classification of NeuN neuron (left, DAPI/NeuN signal; right, Imaris surface rendering) and CD68 phagolysosome interactions in CA3 from 3D confocal microscopy. Scale bar, 5 μm.
(J) The number of CA3 neurons having different CD68 coverage (survey of 1,500–1,989 CA3 neurons from 10 CA3 subfields and n = 5 mice/group). t test (minimal and moderate) or Mann-Whitney test (fully engulfed; dot, one CA3 subfield).
(K) Left: a NeuN neuron reaching "full engulfment" criteria is associated with TMEM119 staining. Scale bar, 10 μm. Right: the proportion of fully engulfed neurons associated with TMEM119 cells (10 CA3 subfields from n = 5 mice).

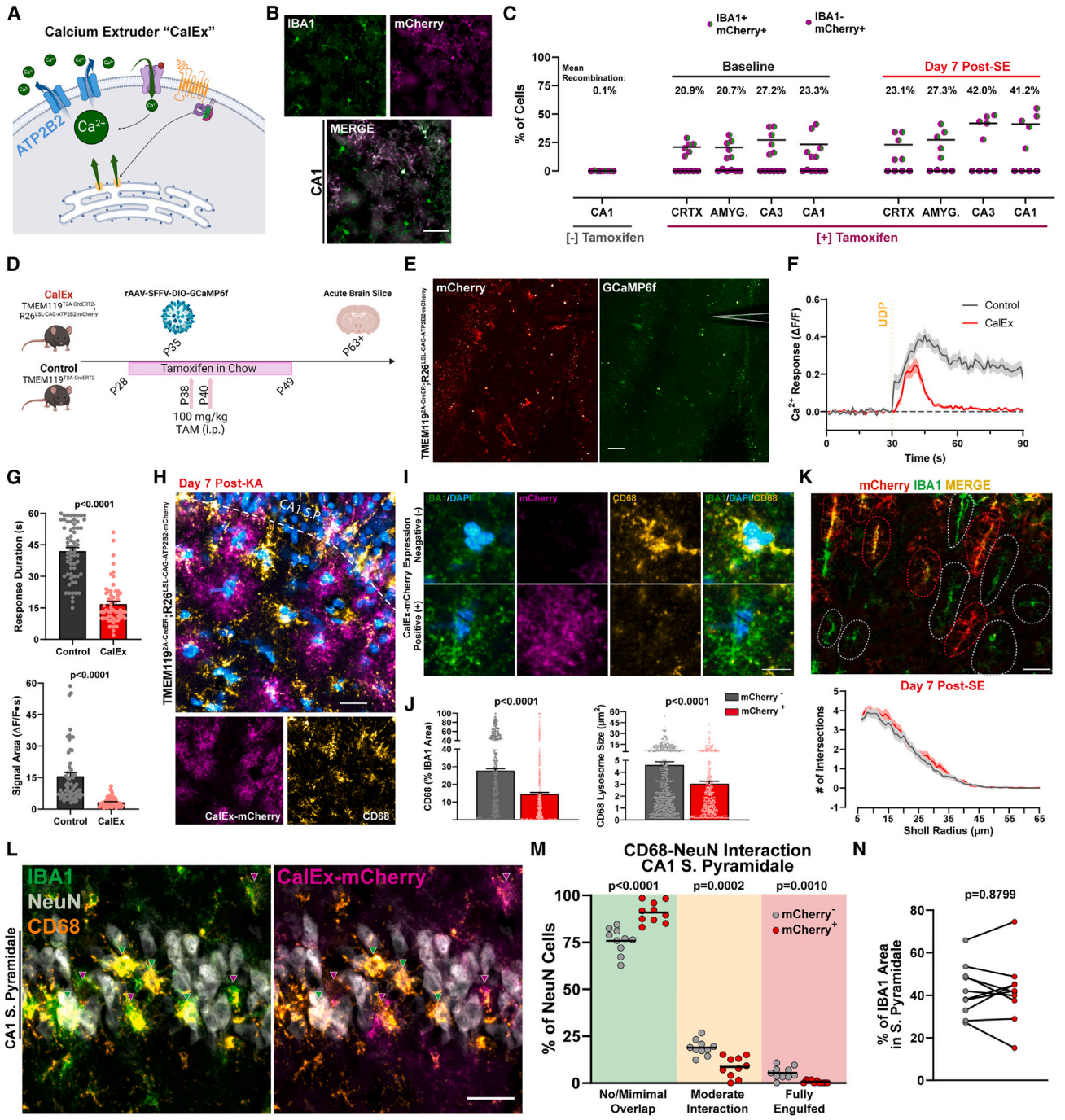

Figure 6. Attenuating calcium signaling through CalEx phenocopies lysosome impairments in microglia

(A) Illustration of ATP2B2 calcium extruder ("CalEx") function.

(B) Images of CalEx-mCherry recombination against an IBA1 co-stain (TMEM119$^{2A\text{-}CreER}$;R26$^{LSL\text{-}CAG\text{-}ATP2B2\text{-}mCherry}$ mice treated with tamoxifen). Scale bar, 30 μm.

(C) Quantification of mean recombination by region (dot, one mouse; n = 5–6 mice per group).

(D) Outline of experimental steps to validate CalEx function in microglia.

(E) Example of mCherry fluorescence and rAAV-SFFV-DIO-GCaMP6f calcium activity following 500 μM focal UDP application (acute CalEx brain slice). Scale bar, 40 μm.

(F) Overall calcium response (ΔF/F) to UDP application (69 responding cells in control tissue and 59 responding cells in CalEx tissue; 2–4 slices from n = 4–5 mice per group).

(G) Quantification of 500 μM UDP calcium response duration, and signal area between control and CalEx microglia. Student's t test (same dataset as F).

(H) Representative image of CalEx-mCherry and CD68 expression in CA1 SR 1 week after KA-SE. Scale bar, 25 μm.

(legend continued on next page)

Please cite this article in press as: Umpierre et al., Microglial P2Y$_6$ calcium signaling promotes phagocytosis and shapes neuroimmune responses in epileptogenesis, Neuron (2024), https://doi.org/10.1016/j.neuron.2024.03.017

and closely related myeloid cells and (2) how the general KO of P2Y$_6$ may affect different myeloid cell populations.

First, the approaches used should be able to successfully identify and distinguish microglial from closely related myeloid cells through the use of a high-parameter panel (flow cytometry), a TMEM119 label or CreER driver[49] (CalEx, RNAscope, and histology), and a Cx3Cr1 CreER driver (calcium imaging; after a 3-week tamoxifen latency).[50] While border-associated macrophage (BAM) populations could also be labeled by the Cx3Cr1^{CreER} system, imaging outside of the meninges, choroid plexus, and vascularized regions should limit the inclusion of BAM populations in the dataset. Therein, most of the studies performed should reasonably select for microglia over outside myeloid cells in analyses.

On the other hand, general KO of the P2Y$_6$ receptor could impact both microglia and outside myeloid populations. Differences in myeloid cell infiltration could occur through multiple potential mechanisms, including direct UDP-based recruitment of P2Y$_6$-expressing myeloid cells (Figure S7). Regardless of mechanism, infiltrating myeloid cells represent a highly pro-inflammatory population (Figure S6). Greater neuron damage/loss in *P2ry6*$^{+/+}$ mice could reasonably reflect the contributions of both microglia and outside myeloid populations to overall tissue inflammation. Future studies will need to utilize conditional KO approaches to better understand the role of microglial versus myeloid P2Y$_6$ signaling in infiltration, tissue inflammation, and cell loss.

UDP1.0 engineering and evaluation of UDP time course

One of the enabling factors contributing to our research is the ability to longitudinally study UDP using a GRAB$_{UDP1.0}$ sensor. UDP signaling is relatively understudied because of issues with antibody specificity[51] and the lack of brain-permeable antagonists.[23] UDP1.0 provides the ability to observe extracellular UDP levels in real time and in a biologically relevant range (10 μM to at least 250 μM). Therein, UDP1.0 could be a valuable tool in studying UDP dynamics during inflections[24] and neurodegeneration.[28–30] UDP1.0 has higher selectivity for UDP over all other purines/pyrimidines tested; however, the sensor may have two limitations to consider, particularly in disease or damage states. First, UDP1.0 can be activated by UTP in the 100–250 μM range (2-Thio-UTP; Figure 2L), a concentration that could reflect extracellular UTP upon cell rupture/membrane damage (UTP$_{IC}$ ≈ 500 μM).[52] Similarly, cell damage could also promote release of intracellular ATP (ATP$_{IC}$ ≈ 3–8 mM)[52,53] at levels that could be sufficient to activate UDP1.0 sensor activity (≥1 mM; Figure 2L). However, it is worth noting that UDP1.0 sensor kinetics are distinctly more rapid when encountering ATP at millimolar levels versus UDP (Figure 2K).

The time course and extent of UDP release cannot entirely explain P2Y$_6$-based microglial calcium signaling in epileptogenesis. While P2Y$_6$ KO attenuates calcium activity over a 7- to 10-day period (Figure 4E), significant elevations in UDP release occur over a shorter time span (3 days in cortex; Figure 3G). Prolonged spontaneous calcium activity could be partially explained by elevated microglial *P2ry6* transcription and UDP calcium sensitivity (Figures 1F–1K). However, it is also possible that early UDP-P2Y$_6$ activation could serve as a "priming" mechanism to engage additional changes in microglial calcium signaling systems. As a damage signal, UDP release is heavily weighted toward periods soon after injury (Figures 3G and 3I), when it could promote early P2Y$_6$/calcium-based transcriptional changes in microglia. Whole-brain transcriptional changes in microglia between genotypes (bulk RNA-seq, day 3; Figures 7A–7C) suggest that most P2Y$_6$-associated transcriptional changes relate to immune function. It will be important to comprehensively understand how different components of microglial immune signaling alter calcium activity and whether P2Y$_6$ calcium elevations could serve to prime or integrate multiple immunological components, including phagocytic systems (e.g., TREM2,[54] TYROBP, Axl, MerTK,[55,56] and Spp1[57]), pattern recognition systems (TLRs), and cytokine response pathways (IFN, IL, and TNF).

How calcium signaling may influence phagocytosis and inflammation

Microglia elevate their calcium signaling in multiple contexts where phagocytosis may be expected: myelin sheath removal,[58] Aβ plaque contact,[59] post-seizure environments,[3] and post-injury environments.[2,5] UDP-P2Y$_6$ signaling has been previously appreciated as a damage recognition system in promoting phagocytosis[24,30] but has not been explicitly studied through the lens of calcium signaling. How calcium activity relates to the overall phagocytic process is unclear but may involve early UDP-P2Y$_6$-based damage recognition and chemotaxis[60] (Figure S4I) or cell migration (Figures S5D and S7) and calcium-based enhancements in lysosome biogenesis (given convergent findings from P2Y$_6$ KO and CalEx approaches). Calcium activity can promote the nuclear translocation of TFEB,[61] a master regulator of lysosome biogenesis. Intracellular calcium is also important for phagosome-lysosome fusion/reformation.[62] Therein, the P2Y$_6$ pathway may contribute to multiple steps in the phagocytic process, including damage recognition, facilitated motility, and lysosome biogenesis.

The P2Y$_6$ pathway may also regulate NF-κB-related inflammation. P2Y$_6$ activation can induce pro-inflammatory cytokine

(I) Closer evaluation of IBA1 and CD68 expression in a representative mCherry$^+$ and mCherry$^-$ cell. Scale bar, 7 μm.
(J) Quantification of average lysosome size and IBA1-normalized CD68 area for mCherry$^+$ and mCherry$^-$ cells. Student's t test (dot, one cell; survey of 412 mCherry$^+$ microglia and 568 mCherry$^-$ microglia in CA1 SR from n = 5 mice/group).
(K) IBA1 morphology in CA1 SR with red and gray outlines denoting mCherry$^+$ and mCherry$^-$ cells, respectively. Scale bar, 20 μm. Sholl plots 1 week after KA-SE (88 mCherry$^+$ and mCherry$^-$ cells from n = 5 mice/group).
(L) Images of the CA1 pyramidal band 7 days after KA-SE, highlighting interactions between neurons and either mCherry$^-$ IBA1 cells (left; green arrows) or mCherry$^+$ IBA1 cells (right; purple arrows) and their associated CD68 expression. Scale bar, 25 μm.
(M) As in Figures 5I and 5J, qualification of NeuN-CD68 interactions in CA1 related to positive or negative mCherry expression. Student's (minimal and moderate) or Welch's (fully engulfed) t test (dot, one region; bilateral CA1 survey from n = 5 mice).
(N) Total IBA1 area within the CA1 pyramidal layer as a percentage of the entire field of view. Paired t test (dot, one region; same dataset as M).
Bar or line graphs display the mean ± SEM.

Please cite this article in press as: Umpierre et al., Microglial P2Y$_6$ calcium signaling promotes phagocytosis and shapes neuroimmune responses in epileptogenesis, Neuron (2024), https://doi.org/10.1016/j.neuron.2024.03.017

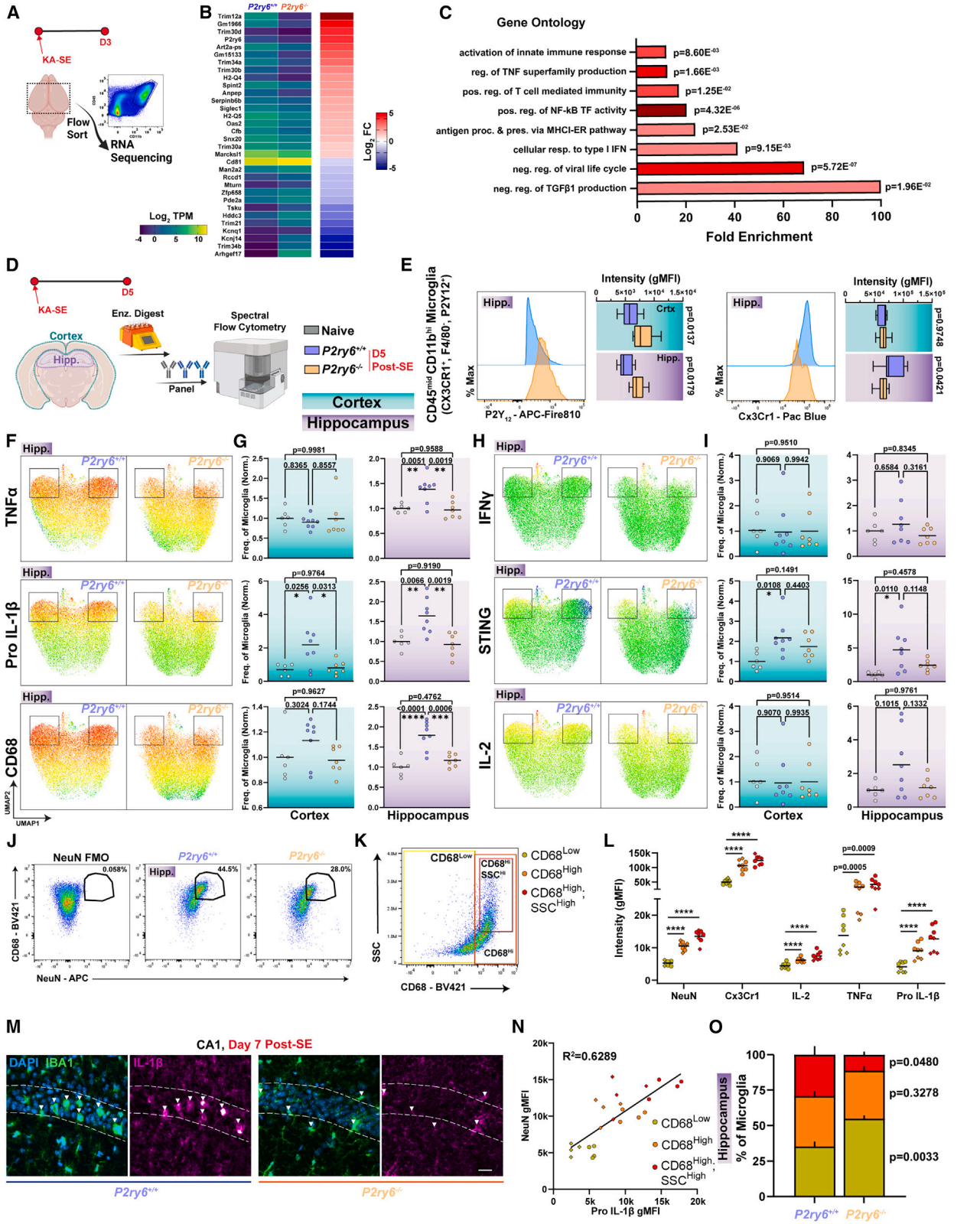

(legend on next page)

Please cite this article in press as: Umpierre et al., Microglial P2Y$_6$ calcium signaling promotes phagocytosis and shapes neuroimmune responses in epileptogenesis, Neuron (2024), https://doi.org/10.1016/j.neuron.2024.03.017

expression in immune cells, but the cytokines created largely depend on the cell type and context.[63–65] Here, we find that murine microglia in an epileptogenic environment increase their production of two major NF-κB cytokines with preserved P2Y$_6$ signaling: IL-1β and TNF-α (Figure 7G). Transcriptomic analyses suggest that P2Y$_6$ signaling may ultimately alter NF-κB activity in microglia through TRIM protein function. In addition, calcium plays multiple known roles in IL-1β signaling, including its cleavage into an active form[66] and its secretion from myeloid cells.[67,68] Genotype-dependent differences in microglial IL-1β expression have perhaps the strongest implications for neuronal degeneration and seizure susceptibility. Various literature[69] have demonstrated that IL-1 antagonism can limit seizure severity[70] or excitotoxicity,[41] while exogenous IL-1 application can increase seizure severity[40] or enhance NMDA calcium entry.[71] Microglia with high-level IL-1β production (Figures 7M and 7N) could secondarily contribute to local neuronal damage during the phagocytic process, particularly in dense neuronal regions like the CA3 SP. We would posit that the known cytotoxic effects of pro-inflammatory cytokines (from both microglial and infiltrating myeloid populations) may explain the continuing evolution of CA3 cell loss and prolonged FJC positivity observed in WT mice that is prevented by P2Y$_6$ KO.

Overall, our results suggest that P2Y$_6$ signaling can enhance neurodegeneration during epileptogenesis through multiple neuroimmune mechanisms, including phagocytic clearance and enhanced local inflammatory signaling.

STAR★METHODS

Detailed methods are provided in the online version of this paper and include the following:

SUPPLEMENTAL INFORMATION

Supplemental information can be found online at https://doi.org/10.1016/j.neuron.2024.03.017.

ACKNOWLEDGMENTS

We thank Dr. Bernard Robaye (Universite Libre de Bruxelles) for the *P2Y6*$^{-/-}$ line and Dr. Alexander Anwar for assistance with image rendering. Institutional access to Imaris and BioRender was provided by the Mayo Foundation. This work was supported by grants from the

Figure 7. Enhanced pro-inflammatory signaling is coordinated with phagocytosis in *P2ry6*$^{+/+}$ microglia

(A) Outline of transcriptomics experiment and microglia isolation 3 days after KA-SE.
(B) Top DEGs in microglia between WT-KO genotypes (log$_2$FC > 1.0 and BH-adjusted p < 0.1).
(C) Key Gene Ontology (GO) terms based upon the DEG set (see STAR Methods).
(D) Protein-level evaluation of hippocampal and cortical microglia using high-parameter flow cytometry.
(E) Mode-normalized histograms and intensity distributions for microglial P2Y$_{12}$ and Cx3Cr1 expression. Two-Way ANOVA with Sidak's post hoc test (boxplots, mean and IQR; whiskers, min to max).
(F) UMAPs of TNF-α, Pro IL-1β, and CD68 expression in hippocampal microglia. Boxes highlight a distinct subpopulation between genotypes (UMAPs: 20,100 microglia per genotype from cohort 2: n = 4 WT, n = 3 KO).
(G) Frequency of TNF-α, Pro IL-1β, and CD68 expression. One-way ANOVA with Tukey's post hoc test (normalized to mean naive frequency per cohort/batch; dot, one mouse).
(H) As in (F), UMAPs of IFNγ, STING, and IL-2 expression in hippocampal microglia.
(I) As in (G), frequency of IFNγ, STING, and IL-2 marker expression.
(J) Pseudocolor plots displaying the NeuN gate, based upon a fluorescence-minus-one (FMO) control, with gating applied to hippocampal microglia.
(K) Pseudocolor plot with gates to isolate microglial populations, which are CD68^{Low}, CD68^{High}, and CD68^{High};SSC^{High}.
(L) Evaluation of signal intensity differences between *P2ry6*$^{+/+}$ hippocampal microglia subpopulations (CD68^{Low}, CD68^{High}, and CD68^{High};SSC^{High}). One-way ANOVA with Tukey's post hoc test (dot, one of three CD68 subpopulation categories from each mouse; dot shape denotes cohort; ****p < 0.0001).
(M) Representative immunofluorescent imaging of DAPI, IBA1, and IL-1β expression in CA1 by genotype. Scale bar, 25 μm.
(N) Correlations between Pro IL-1β intensity and NeuN intensity inside of microglia. Simple linear regression (dot, one mouse).
(O) Comparison of different CD68 population frequencies between genotypes in the hippocampus. Chi-squared test (data represent the mean ± SEM).
Flow cytometry data were aggregated from n = 6 naive mice (4 WT, 2 KO), n = 8 *P2ry6*$^{+/+}$ KA-SE mice, and n = 7 *P2ry6*$^{-/-}$ KA-SE mice across 2 independent cohorts.

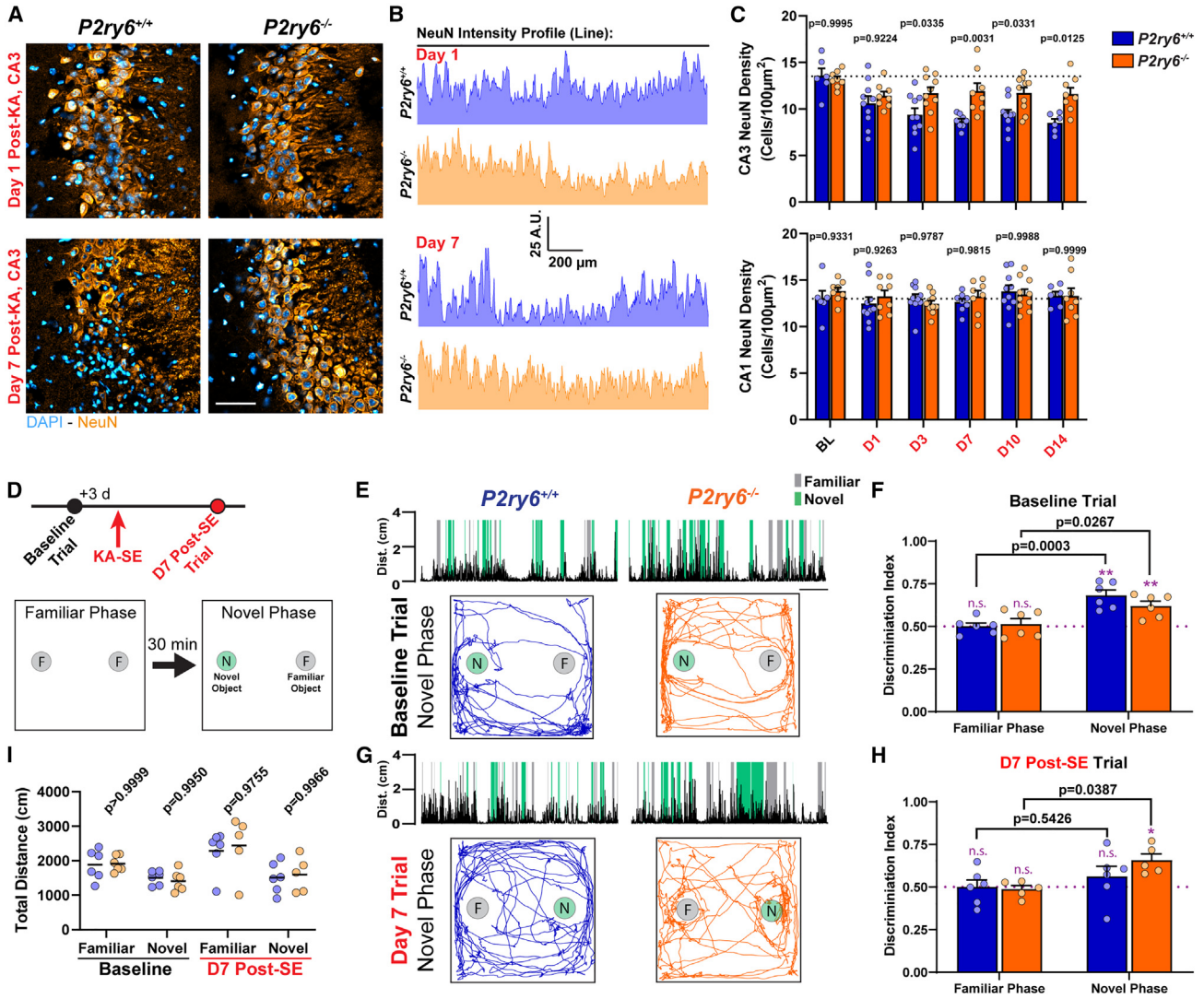

Figure 8. P2Y$_6$ KO mice have improved CA3 neuronal survival and enhanced cognitive task performance

(A) CA3 NeuN and DAPI staining from post-SE WT and KO tissue. Scale bar, 50 µm.

(B) Intensity of the NeuN signal across the CA3 pyramidal band (line plot; see STAR Methods).

(C) Quantification of NeuN cell density in the CA3 or CA1 pyramidal band. Two-way ANOVA with Sidak's post hoc test (dots, one region; bilateral survey from n = 3–5 mice/group).

(D) Timeline of novel object recognition (NOR) task. Outline of the task procedure.

(E) Representative trial performance in the novel phase during the naive test. Top: distance plot overlaid with periods of novel or familiar object interaction. Scale bar, 1 min. Bottom: trace of mouse movement in the arena.

(F) Discrimination index scores during the naive test. Two-way ANOVA with Sidak's post hoc test compares task performance between test phases by genotype (exact p values). One-sample t test compares novel performance against chance: 0.50 (purple text).

(G) As in (E), representative trial performance 7 days after KA-SE.

(H) As in (F), discrimination index 7 days after KA-SE.

(I) Total distance moved by trial phase. Two-Way ANOVA with Sidak's post hoc test (dot, one mouse).

NOR: one cohort of *P2ry6*$^{+/+}$ and *P2ry6*$^{-/-}$ mice tested at baseline and day 7 post-SE (n = 6 mice/group; n = 6/6 surviving *P2ry6*$^{+/+}$; n = 5/6 surviving *P2ry6*$^{-/-}$ at day 7 post-SE).

NIH (K99 NS126417 to A.D.U.; R01 NS103212 and RF1 NS122174 to A.J.J.; and R01 NS088627 and R35 NS132326 to L.-J.W.) and the National Natural Science Foundation of China (31925017 to Y. Li). The funders had no role in study design, data collection and analysis, decision to publish, or preparation of the manuscript.

AUTHOR CONTRIBUTIONS

A.D.U. and L.-J.W. conceptualized the study and wrote the manuscript. B.L., Z.W., and Y. Li created the UDP sensor. A.D.U., S.Z., Y. Liang, and M.X. conducted *in vivo* experiments. K.A. conducted flow cytometry. A.D.U. and G.T.

performed histology and image analysis. W.L.S., M.A.M., and D.B.B. conducted cell culture experiments. J.Z. and S.Z. performed cell isolation. B.H. and J.S. analyzed transcriptomic data. X.Y., A.J.J., Y. Li, and L.-J.W. provided reagents and equipment.

DECLARATION OF INTERESTS

Y. Li is a member of the *Neuron* advisory board.

Received: June 29, 2023
Revised: January 9, 2024
Accepted: March 13, 2024
Published: April 12, 2024

REFERENCES

1. Eichhoff, G., Busche, M.A., and Garaschuk, O. (2008). In vivo calcium imaging of the aging and diseased brain. Eur. J. Nucl. Med. Mol. Imaging *35*, S99–S106. https://doi.org/10.1007/s00259-007-0709-6.
2. Pozner, A., Xu, B., Palumbos, S., Gee, J.M., Tvrdik, P., and Capecchi, M.R. (2015). Intracellular calcium dynamics in cortical microglia responding to focal laser injury in the PC::G5-tdT reporter mouse. Front. Mol. Neurosci. *8*, 12. https://doi.org/10.3389/fnmol.2015.00012.
3. Umpierre, A.D., Bystrom, L.L., Ying, Y., Liu, Y.U., Worrell, G., and Wu, L.J. (2020). Microglial calcium signaling is attuned to neuronal activity in awake mice. Elife *9*, e56502. https://doi.org/10.7554/eLife.56502.
4. Riester, K., Brawek, B., Savitska, D., Fröhlich, N., Zirdum, E., Mojtahedi, N., Heneka, M.T., and Garaschuk, O. (2020). In vivo characterization of functional states of cortical microglia during peripheral inflammation. Brain Behav. Immun. *87*, 243–255. https://doi.org/10.1016/j.bbi.2019.12.007.
5. Eichhoff, G., Brawek, B., and Garaschuk, O. (2011). Microglial calcium signal acts as a rapid sensor of single neuron damage in vivo. Biochim. Biophys. Acta *1813*, 1014–1024. https://doi.org/10.1016/j.bbamcr.2010.10.018.
6. Wu, L.J., Stevens, B., Duan, S., and MacVicar, B.A. (2013). Microglia in neuronal circuits. Neural Plast. *2013*, 586426. https://doi.org/10.1155/2013/586426.
7. Eyo, U.B., Murugan, M., and Wu, L.J. (2017). Microglia-Neuron Communication in Epilepsy. Glia *65*, 5–18. https://doi.org/10.1002/glia.23006.
8. Umpierre, A.D., Bennett, I.V., Nebeker, L.D., Newell, T.G., Tian, B.B., Thomson, K.E., White, H.S., White, J.A., and Wilcox, K.S. (2016). Repeated low-dose kainate administration in C57BL/6J mice produces temporal lobe epilepsy pathology but infrequent spontaneous seizures. Exp. Neurol. *279*, 116–126. https://doi.org/10.1016/j.expneurol.2016.02.014.
9. Puttachary, S., Sharma, S., Thippeswamy, A., and Thippeswamy, T. (2016). Immediate epileptogenesis: Impact on brain in C57BL/6J mouse kainate model. Front. Biosci. *8*, 390–411. https://doi.org/10.2741/e775.
10. Polli, R.S., Malheiros, J.M., Dos Santos, R., Hamani, C., Longo, B.M., Tannús, A., Mello, L.E., and Covolan, L. (2014). Changes in Hippocampal Volume are Correlated with Cell Loss but Not with Seizure Frequency in Two Chronic Models of Temporal Lobe Epilepsy. Front. Neurol. *5*, 111. https://doi.org/10.3389/fneur.2014.00111.
11. Rusina, E., Bernard, C., and Williamson, A. (2021). The Kainic Acid Models of Temporal Lobe Epilepsy. eNeuro *8*, ENEURO.0337-20.2021. https://doi.org/10.1523/ENEURO.0337-20.2021.
12. Shuman, T., Aharoni, D., Cai, D.J., Lee, C.R., Chavlis, S., Page-Harley, L., Vetere, L.M., Feng, Y., Yang, C.Y., Mollinedo-Gajate, I., et al. (2020). Breakdown of spatial coding and interneuron synchronization in epileptic mice. Nat. Neurosci. *23*, 229–238. https://doi.org/10.1038/s41593-019-0559-0.
13. Linden, J., Koch-Nolte, F., and Dahl, G. (2019). Purine Release, Metabolism, and Signaling in the Inflammatory Response. Annu. Rev. Immunol. *37*, 325–347. https://doi.org/10.1146/annurev-immunol-051116-052406.
14. Fukumoto, Y., Tanaka, K.F., Parajuli, B., Shibata, K., Yoshioka, H., Kanemaru, K., Gachet, C., Ikenaka, K., Koizumi, S., and Kinouchi, H. (2019). Neuroprotective effects of microglial P2Y1 receptors against ischemic neuronal injury. J. Cereb. Blood Flow Metab. *39*, 2144–2156. https://doi.org/10.1177/0271678X18805317.
15. Burnstock, G. (2018). Purine and purinergic receptors. Brain Neurosci. Adv. *2*, 2398212818817494. https://doi.org/10.1177/2398212818817494.
16. Masuda, T., Ozono, Y., Mikuriya, S., Kohro, Y., Tozaki-Saitoh, H., Iwatsuki, K., Uneyama, H., Ichikawa, R., Salter, M.W., Tsuda, M., and Inoue, K. (2016). Dorsal horn neurons release extracellular ATP in a VNUT-dependent manner that underlies neuropathic pain. Nat. Commun. *7*, 12529. https://doi.org/10.1038/ncomms12529.
17. Tang, W., Szokol, K., Jensen, V., Enger, R., Trivedi, C.A., Hvalby, Ø., Helm, P.J., Looger, L.L., Sprengel, R., and Nagelhus, E.A. (2015). Stimulation-evoked Ca2+ signals in astrocytic processes at hippocampal CA3-CA1 synapses of adult mice are modulated by glutamate and ATP. J. Neurosci. *35*, 3016–3021. https://doi.org/10.1523/jneurosci.3319-14.2015.
18. Davalos, D., Grutzendler, J., Yang, G., Kim, J.V., Zuo, Y., Jung, S., Littman, D.R., Dustin, M.L., and Gan, W.B. (2005). ATP mediates rapid microglial response to local brain injury in vivo. Nat. Neurosci. *8*, 752–758. https://doi.org/10.1038/nn1472.
19. Umpierre, A.D., West, P.J., White, J.A., and Wilcox, K.S. (2019). Conditional Knock-out of mGluR5 from Astrocytes during Epilepsy Development Impairs High-Frequency Glutamate Uptake. J. Neurosci. *39*, 727–742. https://doi.org/10.1523/JNEUROSCI.1148-18.2018.
20. Panatier, A., and Robitaille, R. (2016). Astrocytic mGluR5 and the tripartite synapse. Neuroscience *323*, 29–34. https://doi.org/10.1016/j.neuroscience.2015.03.063.
21. Sun, W., McConnell, E., Pare, J.F., Xu, Q., Chen, M., Peng, W., Lovatt, D., Han, X., Smith, Y., and Nedergaard, M. (2013). Glutamate-dependent neuroglial calcium signaling differs between young and adult brain. Science *339*, 197–200. https://doi.org/10.1126/science.1226740.
22. Zhang, Y., Chen, K., Sloan, S.A., Bennett, M.L., Scholze, A.R., O'Keeffe, S., Phatnani, H.P., Guarnieri, P., Caneda, C., Ruderisch, N., et al. (2014). An RNA-sequencing transcriptome and splicing database of glia, neurons, and vascular cells of the cerebral cortex. J. Neurosci. *34*, 11929–11947. https://doi.org/10.1523/JNEUROSCI.1860-14.2014.
23. Anwar, S., Pons, V., and Rivest, S. (2020). Microglia Purinoceptor P2Y6: An Emerging Therapeutic Target in CNS Diseases. Cells *9*, 1595. https://doi.org/10.3390/cells9071595.
24. Koizumi, S., Shigemoto-Mogami, Y., Nasu-Tada, K., Shinozaki, Y., Ohsawa, K., Tsuda, M., Joshi, B.V., Jacobson, K.A., Kohsaka, S., and Inoue, K. (2007). UDP acting at P2Y6 receptors is a mediator of microglial phagocytosis. Nature *446*, 1091–1095. https://doi.org/10.1038/nature05704.
25. Steculorum, S.M., Paeger, L., Bremser, S., Evers, N., Hinze, Y., Idzko, M., Kloppenburg, P., and Brüning, J.C. (2015). Hypothalamic UDP Increases in Obesity and Promotes Feeding via P2Y6-Dependent Activation of AgRP Neurons. Cell *162*, 1404–1417. https://doi.org/10.1016/j.cell.2015.08.032.
26. Feng, J., Zhang, C., Lischinsky, J.E., Jing, M., Zhou, J., Wang, H., Zhang, Y., Dong, A., Wu, Z., Wu, H., et al. (2019). A Genetically Encoded Fluorescent Sensor for Rapid and Specific In Vivo Detection of Norepinephrine. Neuron *102*, 745–761.e8. https://doi.org/10.1016/j.neuron.2019.02.037.
27. Smith, D.A., Connick, J.H., and Stone, T.W. (1989). Effect of changing extracellular levels of magnesium on spontaneous activity and glutamate release in the mouse neocortical slice. Br. J. Pharmacol. *97*, 475–482. https://doi.org/10.1111/j.1476-5381.1989.tb11975.x.
28. Dundee, J.M., Puigdellívol, M., Butler, R., Cockram, T.O.J., and Brown, G.C. (2023). P2Y(6) receptor-dependent microglial phagocytosis of synapses mediates synaptic and memory loss in aging. Aging Cell *22*, e13761. https://doi.org/10.1111/acel.13761.
29. Milde, S., van Tartwijk, F.W., Vilalta, A., Hornik, T.C., Dundee, J.M., Puigdellívol, M., and Brown, G.C. (2021). Inflammatory neuronal loss in the substantia nigra induced by systemic lipopolysaccharide is prevented by knockout of the P2Y(6) receptor in mice. J. Neuroinflammation *18*, 225. https://doi.org/10.1186/s12974-021-02280-2.

30. Neher, J.J., Neniskyte, U., Hornik, T., and Brown, G.C. (2014). Inhibition of UDP/P2Y6 purinergic signaling prevents phagocytosis of viable neurons by activated microglia in vitro and in vivo. Glia *62*, 1463–1475. https://doi.org/10.1002/glia.22693.

31. Puigdellívol, M., Milde, S., Vilalta, A., Cockram, T.O.J., Allendorf, D.H., Lee, J.Y., Dundee, J.M., Pampuščenko, K., Borutaite, V., Nuthall, H.N., et al. (2021). The microglial P2Y(6) receptor mediates neuronal loss and memory deficits in neurodegeneration. Cell Rep. *37*, 110148. https://doi.org/10.1016/j.celrep.2021.110148.

32. Yu, X., Taylor, A.M.W., Nagai, J., Golshani, P., Evans, C.J., Coppola, G., and Khakh, B.S. (2018). Reducing Astrocyte Calcium Signaling In Vivo Alters Striatal Microcircuits and Causes Repetitive Behavior. Neuron *99*, 1170–1187.e9. https://doi.org/10.1016/j.neuron.2018.08.015.

33. Yu, X., Moye, S.L., and Khakh, B.S. (2021). Local and CNS-Wide Astrocyte Intracellular Calcium Signaling Attenuation In Vivo with CalEx(flox) Mice. J. Neurosci. *41*, 4556–4574. https://doi.org/10.1523/JNEUROSCI.0085-21.2021.

34. Lin, R., Zhou, Y., Yan, T., Wang, R., Li, H., Wu, Z., Zhang, X., Zhou, X., Zhao, F., Zhang, L., et al. (2022). Directed evolution of adeno-associated virus for efficient gene delivery to microglia. Nat. Methods *19*, 976–985. https://doi.org/10.1038/s41592-022-01547-7.

35. Chang, T.H., Yoshimi, R., and Ozato, K. (2015). Tripartite Motif (TRIM) 12c, a Mouse Homolog of TRIM5, Is a Ubiquitin Ligase That Stimulates Type I IFN and NF-kappaB Pathways along with TNFR-Associated Factor 6. J. Immunol. *195*, 5367–5379. https://doi.org/10.4049/jimmunol.1402064.

36. Uchil, P.D., Hinz, A., Siegel, S., Coenen-Stass, A., Pertel, T., Luban, J., and Mothes, W. (2013). TRIM protein-mediated regulation of inflammatory and innate immune signaling and its association with antiretroviral activity. J. Virol. *87*, 257–272. https://doi.org/10.1128/JVI.01804-12.

37. Yang, W., Gu, Z., Zhang, H., and Hu, H. (2020). To TRIM the Immunity: From Innate to Adaptive Immunity. Front. Immunol. *11*, 02157. https://doi.org/10.3389/fimmu.2020.02157.

38. Pawelec, P., Ziemka-Nalecz, M., Sypecka, J., and Zalewska, T. (2020). The Impact of the CX3CL1/CX3CR1 Axis in Neurological Disorders. Cells *9*, 2277. https://doi.org/10.3390/cells9102277.

39. Vezzani, A., and Baram, T.Z. (2007). New roles for interleukin-1 Beta in the mechanisms of epilepsy. Epilepsy Curr. *7*, 45–50. https://doi.org/10.1111/j.1535-7511.2007.00165.x.

40. Vezzani, A., Conti, M., De Luigi, A., Ravizza, T., Moneta, D., Marchesi, F., and De Simoni, M.G. (1999). Interleukin-1beta immunoreactivity and microglia are enhanced in the rat hippocampus by focal kainate application: functional evidence for enhancement of electrographic seizures. J. Neurosci. *19*, 5054–5065. https://doi.org/10.1523/JNEUROSCI.19-12-05054.1999.

41. Lawrence, C.B., Allan, S.M., and Rothwell, N.J. (1998). Interleukin-1beta and the interleukin-1 receptor antagonist act in the striatum to modify excitotoxic brain damage in the rat. Eur. J. Neurosci. *10*, 1188–1195. https://doi.org/10.1046/j.1460-9568.1998.00136.x.

42. Grbic, D.M., Degagné, É., Larrivée, J.F., Bilodeau, M.S., Vinette, V., Arguin, G., Stankova, J., and Gendron, F.P. (2012). P2Y6 receptor contributes to neutrophil recruitment to inflamed intestinal mucosa by increasing CXC chemokine ligand 8 expression in an AP-1-dependent manner in epithelial cells. Inflamm. Bowel Dis. *18*, 1456–1469. https://doi.org/10.1002/ibd.21931.

43. Dragunow, M., and Robertson, H.A. (1987). Generalized seizures induce c-fos protein(s) in mammalian neurons. Neurosci. Lett. *82*, 157–161. https://doi.org/10.1016/0304-3940(87)90121-2.

44. Dragunow, M., and Robertson, H.A. (1987). Kindling stimulation induces c-fos protein(s) in granule cells of the rat dentate gyrus. Nature *329*, 441–442. https://doi.org/10.1038/329441a0.

45. Antunes, M., and Biala, G. (2012). The novel object recognition memory: neurobiology, test procedure, and its modifications. Cogn. Process. *13*, 93–110. https://doi.org/10.1007/s10339-011-0430-z.

46. Rolls, E.T. (2013). A quantitative theory of the functions of the hippocampal CA3 network in memory. Front. Cell. Neurosci. *7*, 98. https://doi.org/10.3389/fncel.2013.00098.

47. Pennington, Z.T., Diego, K.S., Francisco, T.R., LaBanca, A.R., Lamsifer, S.I., Liobimova, O., Shuman, T., and Cai, D.J. (2021). ezTrack-A Step-by-Step Guide to Behavior Tracking. Curr. Protoc. *1*, e255. https://doi.org/10.1002/cpz1.255.

48. Walz, W., Ilschner, S., Ohlemeyer, C., Banati, R., and Kettenmann, H. (1993). Extracellular ATP activates a cation conductance and a K+ conductance in cultured microglial cells from mouse brain. J. Neurosci. *13*, 4403–4411.

49. Kaiser, T., and Feng, G. (2019). Tmem119-EGFP and Tmem119-CreERT2 Transgenic Mice for Labeling and Manipulating Microglia. eNeuro *6*, ENEURO.0448-18.2019. https://doi.org/10.1523/ENEURO.0448-18.2019.

50. Parkhurst, C.N., Yang, G., Ninan, I., Savas, J.N., Yates, J.R., 3rd, Lafaille, J.J., Hempstead, B.L., Littman, D.R., and Gan, W.B. (2013). Microglia promote learning-dependent synapse formation through brain-derived neurotrophic factor. Cell *155*, 1596–1609. https://doi.org/10.1016/j.cell.2013.11.030.

51. Yu, W., and Hill, W.G. (2013). Lack of specificity shown by P2Y6 receptor antibodies. Naunyn-Schmiedeberg's Arch. Pharmacol. *386*, 885–891. https://doi.org/10.1007/s00210-013-0894-8.

52. Traut, T.W. (1994). Physiological concentrations of purines and pyrimidines. Mol. Cell. Biochem. *140*, 1–22. https://doi.org/10.1007/BF00928361.

53. Zimmerman, M.A., Kam, I., Eltzschig, H., and Grenz, A. (2013). Biological implications of extracellular adenosine in hepatic ischemia and reperfusion injury. Am. J. Transplant. *13*, 2524–2529. https://doi.org/10.1111/ajt.12398.

54. Wang, Y., Cella, M., Mallinson, K., Ulrich, J.D., Young, K.L., Robinette, M.L., Gilfillan, S., Krishnan, G.M., Sudhakar, S., Zinselmeyer, B.H., et al. (2015). TREM2 lipid sensing sustains the microglial response in an Alzheimer's disease model. Cell *160*, 1061–1071. https://doi.org/10.1016/j.cell.2015.01.049.

55. Fourgeaud, L., Través, P.G., Tufail, Y., Leal-Bailey, H., Lew, E.D., Burrola, P.G., Callaway, P., Zagórska, A., Rothlin, C.V., Nimmerjahn, A., and Lemke, G. (2016). TAM receptors regulate multiple features of microglial physiology. Nature *532*, 240–244. https://doi.org/10.1038/nature17630.

56. Lemke, G. (2017). Phosphatidylserine Is the Signal for TAM Receptors and Their Ligands. Trends Biochem. Sci. *42*, 738–748. https://doi.org/10.1016/j.tibs.2017.06.004.

57. De Schepper, S., Ge, J.Z., Crowley, G., Ferreira, L.S.S., Garceau, D., Toomey, C.E., Sokolova, D., Rueda-Carrasco, J., Shin, S.H., Kim, J.S., et al. (2023). Perivascular cells induce microglial phagocytic states and synaptic engulfment via SPP1 in mouse models of Alzheimer's disease. Nat. Neurosci. *26*, 406–415. https://doi.org/10.1038/s41593-023-01257-z.

58. Hughes, A.N., and Appel, B. (2020). Microglia phagocytose myelin sheaths to modify developmental myelination. Nat. Neurosci. *23*, 1055–1066. https://doi.org/10.1038/s41593-020-0654-2.

59. Brawek, B., Schwendele, B., Riester, K., Kohsaka, S., Lerdkrai, C., Liang, Y., and Garaschuk, O. (2014). Impairment of in vivo calcium signaling in amyloid plaque-associated microglia. Acta Neuropathol. *127*, 495–505. https://doi.org/10.1007/s00401-013-1242-2.

60. Wu, L.J., Vadakkan, K.I., and Zhuo, M. (2007). ATP-induced chemotaxis of microglial processes requires P2Y receptor-activated initiation of outward potassium currents. Glia *55*, 810–821. https://doi.org/10.1002/glia.20500.

61. Medina, D.L., Di Paola, S., Peluso, I., Armani, A., De Stefani, D., Venditti, R., Montefusco, S., Scotto-Rosato, A., Prezioso, C., Forrester, A., et al. (2015). Lysosomal calcium signalling regulates autophagy through calcineurin and TFEB. Nat. Cell Biol. *17*, 288–299. https://doi.org/10.1038/ncb3114.

62. Yang, C., and Wang, X. (2021). Lysosome biogenesis: Regulation and functions. J. Cell Biol. *220*, e202102001. https://doi.org/10.1083/jcb.202102001.

63. Cox, M.A., Gomes, B., Palmer, K., Du, K., Wiekowski, M., Wilburn, B., Petro, M., Chou, C.C., Desquitado, C., Schwarz, M., et al. (2005). The pyrimidinergic P2Y6 receptor mediates a novel release of proinflammatory cytokines and

chemokines in monocytic cells stimulated with UDP. Biochem. Biophys. Res. Commun. *330*, 467–473. https://doi.org/10.1016/j.bbrc.2005.03.004.

64. Warny, M., Aboudola, S., Robson, S.C., Sévigny, J., Communi, D., Soltoff, S.P., and Kelly, C.P. (2001). P2Y(6) nucleotide receptor mediates monocyte interleukin-8 production in response to UDP or lipopolysaccharide. J. Biol. Chem. *276*, 26051–26056. https://doi.org/10.1074/jbc.M102568200.

65. Li, S., Li, J., Wang, N., Hao, G., and Sun, J. (2018). Characterization of UDP-Activated Purinergic Receptor P2Y(6) Involved in Japanese Flounder Paralichthys olivaceus Innate Immunity. Int. J. Mol. Sci. *19*, 2095. https://doi.org/10.3390/ijms19072095.

66. Le Feuvre, R.A., Brough, D., Iwakura, Y., Takeda, K., and Rothwell, N.J. (2002). Priming of macrophages with lipopolysaccharide potentiates P2X7-mediated cell death via a caspase-1-dependent mechanism, independently of cytokine production. J. Biol. Chem. *277*, 3210–3218. https://doi.org/10.1074/jbc.M104388200.

67. Brough, D., Le Feuvre, R.A., Wheeler, R.D., Solovyova, N., Hilfiker, S., Rothwell, N.J., and Verkhratsky, A. (2003). Ca2+ stores and Ca2+ entry differentially contribute to the release of IL-1 beta and IL-1 alpha from murine macrophages. J. Immunol. *170*, 3029–3036. https://doi.org/10.4049/jimmunol.170.6.3029.

68. Andrei, C., Margiocco, P., Poggi, A., Lotti, L.V., Torrisi, M.R., and Rubartelli, A. (2004). Phospholipases C and A2 control lysosome-mediated IL-1 beta secretion: Implications for inflammatory processes. Proc. Natl. Acad. Sci. USA. *101*, 9745–9750. https://doi.org/10.1073/pnas.0308558101.

69. Allan, S.M., Tyrrell, P.J., and Rothwell, N.J. (2005). Interleukin-1 and neuronal injury. Nat. Rev. Immunol. *5*, 629–640. https://doi.org/10.1038/nri1664.

70. Vezzani, A., Moneta, D., Conti, M., Richichi, C., Ravizza, T., De Luigi, A., De Simoni, M.G., Sperk, G., Andell-Jonsson, S., Lundkvist, J., et al. (2000). Powerful anticonvulsant action of IL-1 receptor antagonist on intracerebral injection and astrocytic overexpression in mice. Proc. Natl. Acad. Sci. USA. *97*, 11534–11539. https://doi.org/10.1073/pnas.190206797.

71. Viviani, B., Bartesaghi, S., Gardoni, F., Vezzani, A., Behrens, M.M., Bartfai, T., Binaglia, M., Corsini, E., Di Luca, M., Galli, C.L., and Marinovich, M. (2003). Interleukin-1beta enhances NMDA receptor-mediated intracellular calcium increase through activation of the Src family of kinases. J. Neurosci. *23*, 8692–8700. https://doi.org/10.1523/JNEUROSCI.23-25-08692.2003.

72. Martin, M. (2011). Cutadapt removes adapter sequences from high-throughput sequencing reads. EMBnet J. *17*, 10–12. https://doi.org/10.14806/ej.17.1.200.

73. Dobin, A., Davis, C.A., Schlesinger, F., Drenkow, J., Zaleski, C., Jha, S., Batut, P., Chaisson, M., and Gingeras, T.R. (2013). STAR: ultrafast universal RNA-seq aligner. Bioinformatics *29*, 15–21. https://doi.org/10.1093/bioinformatics/bts635.

74. Love, M.I., Huber, W., and Anders, S. (2014). Moderated estimation of fold change and dispersion for RNA-seq data with DESeq2. Genome Biol. *15*, 550. https://doi.org/10.1186/s13059-014-0550-8.

75. Li, B., and Dewey, C.N. (2011). RSEM: accurate transcript quantification from RNA-Seq data with or without a reference genome. BMC Bioinf. *12*, 323. https://doi.org/10.1186/1471-2105-12-323.

76. Wan, Q., Okashah, N., Inoue, A., Nehmé, R., Carpenter, B., Tate, C.G., and Lambert, N.A. (2018). Mini G protein probes for active G protein-coupled receptors (GPCRs) in live cells. J. Biol. Chem. *293*, 7466–7473. https://doi.org/10.1074/jbc.RA118.001975.

77. Racine, R.J. (1972). Modification of seizure activity by electrical stimulation. II. Motor seizure. Electroencephalogr. Clin. Neurophysiol. *32*, 281–294.

78. Ferreira, T.A., Blackman, A.V., Oyrer, J., Jayabal, S., Chung, A.J., Watt, A.J., Sjöström, P.J., and van Meyel, D.J. (2014). Neuronal morphometry directly from bitmap images. Nat. Methods *11*, 982–984. https://doi.org/10.1038/nmeth.3125.

Please cite this article in press as: Umpierre et al., Microglial $P2Y_6$ calcium signaling promotes phagocytosis and shapes neuroimmune responses in epileptogenesis, Neuron (2024), https://doi.org/10.1016/j.neuron.2024.03.017

STAR★METHODS

KEY RESOURCES TABLE

REAGENT or RESOURCE	SOURCE	IDENTIFIER
Antibodies (NEW)		
IBA1 (Rb)	Abcam	Cat#178847; RRID:AB_2832244
IBA1 (Gt)	WAKO	Cat#011-27991; RRID:AB_2935833
TMEM119 (Rb)	Abcam	Cat#209064; RRID:AB_2728083
NeuN (Rb)	Abcam	Cat#177487; RRID:AB_2532109
NeuN (Ms)	Abcam	Cat#104224; RRID:AB_10711040
CD68 (Rb)	Abcam	Cat#125212; RRID:AB_10975465
CD68 (Rt)	Abcam	Cat#53444; RRID:AB_869007
LAMP1 (Rb)	Abcam	Cat#208943; RRID:AB_2923327
IL-1β (Ms)	CST	Cat#12242S; RRID:AB_2715503
cFOS (Rb)	CST	Cat#2250S; RRID:AB_2247211
CD45-PerCP	Biolegend	Cat#103130; RRID:AB_893343
CD11b-BV650	Biolegend	Cat#101239; RRID:AB_11125575
CD11b-PE/Cy5	Tonbo (Cytek)	Cat#55-0112-U100; RRID:AB_2621818
CD126-BUV563	BD	Cat#741296; RRID:AB_2870824
MERTK-BV786	BD	Cat#747890; RRID:AB_2872352
CD25-BV750	BD	Cat#747331; RRID:AB_2872035
CX3CR1-PacificBlue	Biolegend	Cat#149038; RRID:AB_2632858
P2Y12-APC-Fire810	Biolegend	Cat#848013; RRID:AB_2904450
TCRβ-PE/Cy7	Tonbo (Cytek)	Cat#60-5961-U100; RRID:AB_2877098
CD11c-SPARK-NIR-685	Biolegend	Cat#117368; RRID:AB_2894416
Ly6G-BV711	Biolegend	Cat#127643; RRID:AB_2565971
CD4-BV510	Biolegend	Cat#100559; RRID:AB_2562608
CD8α-BV570	Biolegend	Cat#100740; RRID:AB_2563055
CD122-BB700	BD	Cat#742153; RRID:AB_2740663
F4/80-BUV395	BD	Cat#565614; RRID:AB_2739304
NK1.1-BUV615	BD	Cat#751111; RRID:AB_2875140
MHCII-BUV805	BD	Cat#748844; RRID:AB_2873247
NeuN-APC	Novus	Cat#NBP1-92693APC; RRID:AB_2894834
Vimentin-CL488	Thermo	Cat#CL488-60330; RRID:AB_2883145
TNFα-BV650	Biolegend	Cat#506333; RRID:AB_2562450
Pro-IL1β-PE	Thermo	Cat#12-7114-82; RRID:AB_10732630
CD68-BV421	BD	Cat#566389; RRID:AB_2744447
STING-PE/CF594	BD	Cat#565313; RRID:AB_2739176
IL2-BV605	BD	Cat#563911; RRID:AB_2738482
IFNγ-BUV737	BD	Cat#612769; RRID:AB_2870098
Bacterial and virus strains		
AAV2/9-hSyn-UDP1.0	This paper, Brain VTA	Cat#PT-7072
rAAV-MG1.2-SFFV-DIO-GCaMP6f-WPRE-hGH-polyA	Brain VTA/Biohippo	Cat#PT-6329
Chemicals, peptides, and recombinant proteins		
Zombie UV	Biolegend	Cat#423107
UDP disodium salt	Tocris	Cat#3111
ATP disodium salt	Tocris	Cat#3245

(*Continued on next page*)

Please cite this article in press as: Umpierre et al., Microglial P2Y$_6$ calcium signaling promotes phagocytosis and shapes neuroimmune responses in epileptogenesis, Neuron (2024), https://doi.org/10.1016/j.neuron.2024.03.017

Continued

REAGENT or RESOURCE	SOURCE	IDENTIFIER
2-ThioUTP tetrasodium salt	Tocris	Cat#3280
2-MethylthioADP trisodium salt	Tocrs	Cat#1624
MRS-2693 trisodium salt	Tocris	Cat#2502
MRS-2578	Tocris	Cat#2146
Kainic Acid	Tocris	Cat#0222
Valproic Acid, Sodium Salt	Millipore-Sigma	Cat#P4543
Alexa Fluor 568 Dye	Invitrogen	Cat#A33081
Calbryte-590 a.m.	AAT Bioquest	Cat#20702-AAT
PPADS	Cayman	Cat#14537
Suramin	Cayman	Cat#11126
Apyrase grade VII	Millipore-Sigma	Cat#A6535
CCL2	R&D Systems	Cat#479-JE
Critical commercial assays		
Tumor Dissociation Kit	Miltenyi	Cat#130-095-942
Adult Brain Dissociation Kit	Miltenyi	Cat#130-107-677
Macrophage Isolation Kit	Miltenyi	Cat#130-110-434
RNAscope Multiplex v2	ACD	Cat#323100
SMART SEQ II kit	Takara	Cat#634411
Transwell Insert (6.5 mm, 8 μm)	Corning	Cat#3422
Deposited data		
Bulk RNA-seq	This paper	SRA: PRJNA982384
Experimental models: Cell lines		
HEK293T	ATCC	Cat#CRL-3216
Experimental models: Organisms/strains		
C57BL6/J (WT)	The Jackson Laboratory	Cat#000664; RRID:IMSR_JAX:000664
P2ry6$^{-/-}$	Dr. B. Robaye (ULB)	MGI:4941862
Cx3Cr1$^{CreER-IRES-eYFP}$	The Jackson Laboratory	Cat#021160; RRID:IMSR_JAX:021160
R26$^{LSL-CAG-GCaMP6s}$ (Ai96)	The Jackson Laboratory	Cat#024106; RRID:IMSR_JAX:024106
R26$^{LSL-CAG-ATP2B2-mCherry}$ (CalEx)	Dr. X. Yu (Univ. Illinois, Urbana-Champaign)	Cat#035252; RRID:IMSR_JAX:035252
TMEM119$^{2A-CreERT2}$	The Jackson Laboratory	Cat#031820; RRID:IMSR_JAX:031820
Oligonucleotides		
Tmem119 Probe	ACD	Cat#472901 (C1); Mm-TMEM119
P2ry6 Probe	ACD	Cat#314241-C2; Mm-P2ry6-C2
Aldh1l1 Probe	ACD	Cat#405891-C3; Mm-Aldh1l1-C3
Rbfox3 Probe	ACD	Cat#313311-C4; Mm-Rbfox3-C4
Ccr2 Probe	ACD	Cat#501681-C3; Mm-Ccr2-O1-C3
Ptprc Probe	ACD	Cat#412331-C4; Mm-Ptprc-noXHs-C4
Software and algorithms		
ImageJ (1.53t)	NIH	https://imagej.nih.gov/ij/download.html
Prism (V9.5.1)	Graph Pad	https://www.graphpad.com/
ezTrack	Pennington et al.[48]	https://github.com/denisecailab/ezTrack
FloJo (V9)	BD	https://www.flowjo.com/
Imaris (V10.0.0)	Oxford/Bitplane	https://imaris.oxinst.com/
Cutadapt	Martin et al.[72]	https://cutadapt.readthedocs.io/en/stable/
STAR (V.2.5.4b)	Dobin et al.[73]	https://github.com/alexdobin/STAR
DESeq2 (V1.30.1)	Love et al.[74]	https://bioconductor.org/packages/release/bioc/html/DESeq2.html

(*Continued on next page*)

Please cite this article in press as: Umpierre et al., Microglial $P2Y_6$ calcium signaling promotes phagocytosis and shapes neuroimmune responses in epileptogenesis, Neuron (2024), https://doi.org/10.1016/j.neuron.2024.03.017

Continued

REAGENT or RESOURCE	SOURCE	IDENTIFIER
RSEM (V1.3.1)	Li et al.[75]	https://github.com/deweylab/RSEM
Other		
Tamoxifen chow (500 mg TAM per 1 kg chow)	Envigo	Cat#TD.130858

RESOURCE AVAILABILITY

Lead contact

Further information and requests for resources and reagents should be directed to and will be fulfilled by the Lead Contact, Long-Jun Wu (longjun.wu@uth.tmc.edu).

Materials availability

The AAV2/9-hSyn-UDP1.0 virus generated in this study has been deposited to BrainVTA (PT-7072).

Data and code availability

- Bulk RNA-seq data have been deposited at SRA and are publicly available. Accession numbers are listed in the key resources table. All other data reported in this paper will be shared by the lead contact upon reasonable request.
- This paper does not report original code.
- Any additional information required to reanalyze the data reported in this paper is available from the lead contact upon request.

EXPERIMENTAL MODEL AND SUBJECT DETAILS

Animals

P2ry6$^{-/-}$ mice were kindly provided by Dr. Bernard Robaye of the University of Brussels (ULB). CalEx mice (R26$^{\text{LSL-CAG-ATP2B2-mCherry}}$) were provided by Dr. Xinzhu Yu (University of Illinois Urbana-Champaign). C57BL/6J (WT) mice, Cx3Cr1$^{\text{CreER-IRES-eYFP}}$ mice, TMEM119$^{\text{2A-CreERT2}}$ mice, and R26$^{\text{LSL-CAG-GCaMP6s}}$ mice were obtained from The Jackson Laboratory. Male and female mice were used in all studies, with procedures beginning at an age of 5 weeks. To mitigate the impact of background genetics in experiments, *P2ry6*$^{-/-}$ mice were crossed with in-house C57BL/6 mice to obtain *P2ry6*$^{+/-}$ mice. These mice were then intercrossed to generate *P2ry6*$^{+/+}$ and *P2ry6*$^{-/-}$ breeders for all non-imaging experiments. For microglial calcium imaging experiments, we similarly derived *P2ry6*$^{+/+}$;Cx3Cr1$^{\text{CreER-IRES-eYFP/WT}}$;R26$^{\text{LSL-CAG-GCaMP6s/WT}}$ and *P2ry6*$^{-/-}$;Cx3Cr1$^{\text{CreER-IRES-eYFP/WT}}$;R26$^{\text{LSL-CAG-GCaMP6s/WT}}$ lines from an intercross. Animals were group-housed on a 12h light-dark cycle in a temperature- and humidity-controlled room. To induce recombination, mice were weaned at P21 and given free access to tamoxifen in chow (500 mg tamoxifen/1 kg chow) for two- or four-weeks in their home cage. Tamoxifen-restricted littermates were separated at random during weaning and provided a standard diet during this period. Otherwise, assignment was based upon genotype and was therefore not randomized. However, investigators were blinded to genotype during experiments. Animal procedures were in agreement with NIH and Institutional Animal Care and Use Committee (IACUC) guidelines. Protocols were approved by the Mayo Clinic IACUC.

Cell lines

HEK293T cells were obtained from ATCC. All cell lines were cultured at 37°C in DMEM (Biological Industries) with 5% CO_2, supplemented with 10% (v/v) fetal bovine serum (FBS; GIBCO) and 1% penicillin-streptomycin (PS; Biological Industries).

METHOD DETAILS

Molecular biology

To develop a UDP sensor, we inserted the cpEGFP module from $GRAB_{NE1m}$ (containing flanking peptide linkers) into the chicken $P2Y_6$ receptor. We screened TM5 insertion sites ranging from L214$^{5.65}$ to V225$^{6.26}$, and TM6 insertion sites from G221$^{6.23}$ to M235$^{6.36}$. All sensor variants were generated by overlap PCR without cloning into an expression plasmid. The forward primer is upstream of the CMV promoter-sensor-IRES-mCherry-CAAX-polyA expression cassette, amplifying a fragment containing the C-terminal half of $cP2RY_6$ with IRES-mCherry-CAAX-polyA. The reverse primer targeted the TM5 insertion site using a 20–30 bp sequence homologous to the linker in the cpEGFP module from $GRAB_{NE1m}$. This permitted the amplification of a fragment containing CMV promoter and N-terminal half of *cP2ry6*. A third DNA fragment was amplified containing the cpGFP module from $GRAB_{NE1m}$. By performing overlap PCR, these 3 fragments were joined into a complete expression cassette. For the purpose of optimization, candidate sensor variants with known sequence alterations (i.e., truncation variants, point-mutation variants) were sequentially screened. To

Please cite this article in press as: Umpierre et al., Microglial $P2Y_6$ calcium signaling promotes phagocytosis and shapes neuroimmune responses in epileptogenesis, Neuron (2024), https://doi.org/10.1016/j.neuron.2024.03.017

optimize the signal (Figure S3A), we truncated the N-terminal linker of the cpEGFP module by 49 amino acids and the C-terminal linker by 2 amino acids. Additionally, four mutations were introduced at the interface between the cpEGFP module and the chicken $P2Y_6$ sequence to produce $GRAB_{UDP1.0}$. PCR reactions were conducted with a high-fidelity 2x PCR mix (Vazyme, P510-01). A final concentration of 1 M betaine and 1 mM DTT was added to the PCR mixture to improve specificity. Plasmids were generated using a Gibson assembly. DNA fragments were generated using PCR amplification with primers containing ~25 bp overlap (XianghongShengwu, Beijing). All sequences were verified through Sanger sequencing by RuiboXingke (Beijing). The plasmids used to express the $GRAB_{UDP1.0}$ sensor in HEK293T cells were based on the pDisplay vector, with an IgK secretion signal peptide added to the N-terminal of $GRAB_{UDP1.0}$, following the IRES-mCherry-CAAX sequence, to ensure cell membrane labeling with RFP. The plasmid used to express the $GRAB_{UDP1.0}$ sensor in mammalian neurons was cloned into a pAAV vector under the control of the hSyn promoter.

Expression of $GRAB_{UDP}$ variants in cultured cells

For the purpose of library screening, HEK293T cells expressing candidate $GRAB_{UDP}$ sensor variants were seeded in 96-well plates (PerkinElmer). 1–2 μL PCR product mixed with 0.9 μL PEI MAX (Polyscience, 24765-100) was directly transfected into HEK293T cells in the 96-well plate. Following 12-h transfection, the culture medium was replaced. Imaging or functional testing was performed after an additional 24–36 h. For $GRAB_{UDP1.0}$ *in vitro* characterization, 300 ng of plasmid was transfected per well into 96-well plates containing HEK293T cells following the time course of the library screening.

Confocal imaging of cultured cells

Before imaging, culture media was replaced with Tyrode's solution containing (in mM): 150 NaCl, 4 KCl, 2 MgCl2, 2 CaCl2, 10 HEPES, and 10 glucose (pH 7.3–7.4). HEK293T cells grown in 96-well plates were imaged using an Opera Phoenix high-content, confocal screening system (PerkinElmer) equipped with a 20x/0.4 NA objective, a 40×/0.6 NA objective, and a 40×/1.15 NA water-immersion objective, with 488-nm and 561-nm laser lines. Green fluorescence and red fluorescence were passed through 525/50-nm and 600/30-nm emission filters, respectively. Cells grown on 12-mm coverslips were imaged using a Ti-E A1 confocal microscope (Nikon) equipped with a 10x/0.45 NA objective, a 20×/0.75 NA objective, and a 40×/1.35 NA oil-immersion objectives, with 488-nm and 561-nm laser lines. Green fluorescence ($GRAB_{UDP}$), and red fluorescence (mCherry-CAAX) were passed through 525/50-nm and 595/50-nm emission filters, respectively.

Spectrum measurement

HEK293T cells were propagated in a 6-well dish, maintaining a seeding density of 2.6 x 10^5 cells. Cells were then transfected using 4 μg of pDisplay-UDP1.0-IRES-mCherry plasmid. Following standard cell culture procedures, cells were detached using a 2.5% Trypsin solution and resuspended in 1 mL of DMEM with 10% FBS and 1% PS. Subsequently, cells were rinsed twice with Tyrode's solution and resuspended in a final volume of 500 μL Tyrode's solution. A 30 μL aliquot of cell suspension was placed into a 384-well microplate (Corning, CLS4514) for spectrum analysis using TECAN safire2. We recorded the excitation spectrum using a fixed emission filter at 540 ± 10 nm, scanning the excitation wavelength from 385 nm to 520 nm with a 10 nm bandwidth filter. The emission spectrum was measured with a fixed excitation wavelength at 470 ± 10 nm, scanning the emitted light from 495 to 600 nm with a 10 nm bandwidth filter. To acquire the maximum fluorescence of $GRAB_{UDP1.0}$, we added a final concentration of 100 μM UDP to the cell suspension. To acquire the minimum fluorescence, 5 U/mL of apyrase VII (Sigma) was added to deplete any potential basal UDP. Measurement of non-transfected HEK293T cells at a similar density served as a control. We recorded data from three wells for each condition.

Luciferase complementation assay

The split-luciferase complementation assay was performed as previously described.[76] Briefly, 96-well cultured HEK293T cells were transfected with either cP2Y6-SmBit and LgBit-mGq (cP2Y6), UDP1.0-Smbit and LgBit-mGq (UDP1.0), or LgBit-mGq alone (Control). 24 h after transfection, DMEM with 10% FBS and 1% PS was replaced by Tyrode's solution. UDP (at concentrations ranging from 1 nM to 1 mM) was then applied with a final concentration of 5 μM furimazine (NanoLuc Luciferase Assay, Promega). Luminescence was subsequently measured using a Victor X5 multi-label plate reader (PerkinElmer).

Induction of kainate status epilepticus (KA-SE)

Kainic acid was dissolved at 2 mg/mL in sterile saline (0.9%) and stored at room temperature for up to 3 weeks. Kainate was administered to mice without surgery at 5–9 weeks of age, or 3–5 weeks post-surgery. Mice received a first dose of 17.5 mg/kg KA (i.p.). Mice which did not display a Racine stage 4–5 seizure[77] in the first hour were administered an additional 7.5 mg/kg (i.p.) injection every 30 min until a first Racine stage 4–5 seizure. After a first seizure, if mice did not display a Racine stage 4–5 seizure for 30 min, they were administered an additional 7.5 mg/kg injection. This process was followed until mice displayed 8 Racine stage 4–5 seizures. After the 8^{th} seizure, mice were administered valproic acid (250 mg/kg, i.p.) to attenuate SE. To mitigate the risk of batch variability and achieve more consistent neuropathology, we set inclusion/exclusion criteria based on initial seizure burden (defined as the sum of all Racine 4/5 seizures experienced during KA-SE; e.g., 8 Racine stage 5 seizures correspond to a seizure burden of 40). Specifically, mice needed to experience between 8 and 12 Racine stage 4/5 seizures in total. Mice with seizure burdens above or

below this range were excluded. Following valproic acid administration, behavioral seizure monitoring was discontinued once 30 min had elapsed from the timing of the last seizure.

Viral transfection

At least 1 h prior to surgery, adult mice (5–8 weeks) were administered 5 mg/kg carprofen (s.c.) and 4 mg/kg dexamethasone (s.c.). Mice were then anesthetized with 3% isoflurane, shaved, and transferred into a stereotaxic frame (David Kopf Instruments), where an anesthetic plane was maintained with 1.0–2.0% isoflurane throughout surgery. To image longitudinal UDP release events *in vivo*, the skin overlaying the skull was cut away with scissors in a circular pattern and the pericranium was removed by peroxide. C57BL/6J WT mice were then injected through a drilled burr hole with AAV2/9-hSyn-UDP1.0 (titer: $2.9x10^{12}$ GC/mL), targeting layer 5 and layer 2/3 of somatosensory cortex (at 500 μm and 200 μm below the dura, respectively). A total of 250 nL AAV was dispensed at each cortical layer through a glass-capillary-attached Hamilton syringe at a rate of 40 nL/min using an UltraMicroPump-4 system (World Precision Instruments). To image UDP in hippocampus, we performed a midline incision of the scalp and performed stereotaxic AAV injection in C57BL/6J mice. We created a bilateral burr hole at AP: −1.8; ML: ±2.3 and slowly (1 mm/min) lowered a glass microcapillary to the level of CA3b (DV: −2.1 relative to bregma). Both hippocampi were infused with 700 nL of AAV2/9-hSyn-UDP1.0 ($1.5x10^{12}$ GC/mL) at 100 nL/min. After waiting 10 min post-infusion, the microcapillary was slowly raised and the midline incision was sealed with Vetbond (3M). To validate CalEx function, $TMEM119^{2A\text{-}CreERT2}$; $R26^{LSL-CAG\text{-}ATP2B2-mCherry}$ mice and $TMEM119^{2A\text{-}CreERT2}$ mice were injected with rAAV-SFFV-DIO-GCaMP6f-WPRE-hGH-polyA (titer: $2.4x10^{12}$ GC/mL; Biohippo PT-6329). Bilateral injections were performed targeting the CA1 S.R. (500 nL at 100 nL/min; AP: −1.8; ML: ±1.5; DV: −1.4 relative to bregma). The midline incision was sealed with Vetbond. To ensure viral expression under the $TMEM119^{2A\text{-}CreERT2}$ system, mice were fed tamoxifen chow for two weeks, beginning one week prior to viral transfection. In addition, a 100 mg/kg (i.p.) tamoxifen injection in corn oil was administered 3 and 5 days post-surgery.

Cranial window surgery

For mice undergoing UDP1.0 transfection in cortex for *in vivo* imaging, the cranial window was installed during the transfection surgery. After UDP1.0 injection, a 3 mm circular craniotomy was created around the center of the injection site and the bone flap was carefully removed with fine forceps without tearing the dura. After bleeding was carefully resolved, a 3 mm circular coverslip (#0 thickness, Warner Instruments) was placed into the craniotomy and secured with blue-light curing dental glue (Tetric Evoflow, Ivoclar). Dental primer was then applied to the skull surface (iBond Total Etch, Kulzer) before a 4-point headpiece (Model 2, Neurotar) was secured in place with blue-light curing dental glue, sealing the entire skull surface. For studies of spontaneous calcium activity *in vivo*, $CX_3CR1^{CreER\text{-}IRES\text{-}eYFP}$;$R26^{LSL\text{-}CAG\text{-}GCaMP6s}$ mice, which were either $P2ry6^{+/+}$ or $P2ry6^{-/-}$, underwent cranial window surgery without viral transfection.

In vivo 2-photon imaging

All *in vivo* imaging was performed at least 4 weeks after cranial window surgery (with or without viral transfection) to mitigate the impact of post-surgical inflammation and allow for robust viral transfection (if applicable). Prior to imaging, mice were acclimated to head fixation once daily for three days (15 min sessions) prior to the first imaging experiments. All imaging was performed in awake, head-fixed mice, which were able to ambulate on a floating platform (Neurotar Mobile Home Cage). Multiphoton imaging was conducted with a Scientifica Vista scope equipped with multi-Alkali photomultiplier tube detectors and galvo-galvo scanning. Excitation was achieved through a Mai Tai DeepSee laser, tuned to 940 nm for GCaMP6s or UDP1.0 imaging. Laser power under the objective was kept below 50mW during imaging. Green channel emission was passed through a 525 ± 50 filter. Spontaneous microglia calcium activity was captured as a 15 min T-series from a 300 × 300 μm area (512 x 512 pixels) at a 1Hz frame rate using a water immersion objective (Nikon, 16×; NA:0.8). A larger field of view (620 × 620 μm) and longer acquisition time (30 min) was used for UDP1.0 imaging. All *in vivo* imaging was performed 50–175 μm below the dura in the somatosensory cortex.

Brain slice preparation

Mice (6–9 weeks of age) were deeply anesthetized by isoflurane anesthesia (drop method, bell jar). After decapitation, the head was immediately cooled by submersion in ice-cold sucrose solution (185 mM sucrose, 2.5 mM KCl, 1.2 mM NaH_2PO_4, 25 mM $NaHCO_3$, 25 mM glucose, 10 mM $MgSO_4$, and 0.5 mM $CaCl_2$, bubbled with 95% oxygen and 5% CO_2 with an adjusted pH of 7.35–7.42 and an osmolarity of 280–290 mOsm/kg). The brain was then rapidly removed and 350 μm coronal sections were obtained via vibratome (Leica VT1000S), using the same ice-cold sucrose solution. Slices were rinsed in artificial cerebrospinal fluid (aCSF) before transfer to a recovery chamber containing 34°C aCSF (126 mM NaCl, 2.5 mM KCl, 1 mM NaH_2PO_4, 26 mM $NaHCO_3$, 10.5 mM glucose, 1.3 mM $MgSO_4$, and 2 mM $CaCl_2$, bubbled with 95% oxygen and 5% CO_2 with an adjusted pH of 7.35–7.42 and an osmolarity of 298–310 mOsm/kg). Slices were incubated at 34°C for 20 min then allowed to return to room temperature for 10 min prior to use. Slices were imaged using the same multiphoton system, equipped with a custom-made slice perfusion system (maintained at a 1–3 mL/min flow rate using room temperature aCSF). Reagents for extracellular solutions were acquired from Millipore-Sigma. All *ex vivo* imaging was performed at least 50 μm below the slice surface.

Please cite this article in press as: Umpierre et al., Microglial $P2Y_6$ calcium signaling promotes phagocytosis and shapes neuroimmune responses in epileptogenesis, Neuron (2024), https://doi.org/10.1016/j.neuron.2024.03.017

Two-photon studies and analyses

Evaluation of spontaneous calcium activity

Spontaneous microglial calcium levels were assessed in *P2ry6*$^{+/+}$;Cx3Cr1$^{CreER\text{-}IRES\text{-}eYFP}$;R26$^{LSL\text{-}CAG\text{-}GCaMP6s}$ and *P2ry6*$^{-/-}$;Cx3Cr1$^{CreER\text{-}IRES\text{-}eYFP}$;R26$^{LSL\text{-}CAG\text{-}GCaMP6s}$ mice. Two T-series per mouse (900 fames) were captured from non-overlapping locations under the window and followed longitudinally for up to 14 days. T-series were processed in ImageJ by first correcting drift using subpixel registration through the Template Matching plugin. To establish somatic microglial ROIs, the user manually outlined these structures in an average intensity projection from the full field of view. Mean pixel intensity was captured from somatic ROIs using the multi-measure tool. Somatic ROIs were then masked in the average intensity image to decouple this region from microglial processes. Process ROIs could then be extracted from the average intensity image by thresholding the remaining image data and similarly using the multi-measure tool to capture mean pixel intensity in the T series. To mitigate selection bias, ROIs could only be selected from the average intensity image, which most strongly reflects the weak, constitutive eYFP fluorophore in microglia ($CX_3CR1^{CreER\text{-}IRES\text{-}eYFP}$) over GCaMP6s calcium dynamics. Mean pixel intensities for each ROI were converted to $\Delta F/F_0$ values through an Excel template by establishing the mean fluorescence for each of nine 100-frame intervals, then setting the F_0 term as the lowest, non-negative 100-frame average. A calcium signal was considered significant at a $\Delta F/F$ level 3x greater than its standard deviation above baseline. The baseline is the average $\Delta F/F$ value in the lowest 100-frame interval while the standard deviation is calculated across all frames. Any and all frames above this threshold were summated to acquire the ROI's calcium signal area ($\Delta F/F \cdot s$). For *ex vivo* spontaneous calcium imaging, the same genotypes and parameters (300 × 300 μm field of view, 1Hz, 15 min) were utilized. Spontaneous calcium activity in slice was processed and analyzed nearly identically to *in vivo* datasets, except for an additional correction step. If Z drift was minimal (microglial processes may shift but are not lost from the field of view; <4 μm), the raw trace was corrected by fitting a linear slope to the drift and normalizing each frame against the slope term and frame number. This correction was not applied to ROIs which had a calcium event at the start or end of the recording. If Z drift was >4 μm, assessed immediately after acquisition, we performed video re-capture.

Evaluation of UDP release

After X/Y correction with the moco plugin, UDP events were manually identified from T-series by two independent investigators with strong congruency. UDP events were not uniformly radial, so their areas were outlined using the freeform tool to create ROIs, followed by ImageJ ROI area and X/Y-location (centroid) measurement. To obtain fluorescent values, mean fluorescent intensity was acquired through the multi-measure tool. To convert fluorescent intensity values into $\Delta F/F_0$ values, the F_0 term was set as the median fluorescence in the 60 frames preceding event start. Event start was defined manually as the first frame preceding rise kinetics. The event end was calculated with a 10-frame moving window average. The first frame of the smoothed average which reached the F_0 value was considered the event end. These frame values were used to define event time. A summation of $\Delta F/F$ values between these time points yielded the $\Delta F/F \cdot s$ signal area for an event. A summation of $\Delta F/F \cdot s$ signal areas from all events occurring within a 30 min acquisition was termed the cumulative signal area. *Ex vivo* UDP biosensor imaging occurred under identical settings (620 × 620 μm field of view, 1Hz, 15–30 min) for both the cortex and CA3 region. To compare *ex vivo* and *in vivo* UDP dynamics (Figures S2A–S2C), *in vivo* sensor imaging in cortex, at a depth 60–120 μm below the dura (approximately layers I to II/III), was compared to imaging of layers I to II/III in a coronal slice (>60 μm below the cut surface). To induce epileptiform activity in slice, we perfused in daily aCSF lacking $MgSO_4$. Both external solutions were corrected to have identical pH and an osmolarity within ±3 mOsm.

Evaluation of agonist calcium responses

Agonists were locally dispensed through a glass capillary at 3–5 psi for 300–600 ms using a Pico-spritzer III board (Parker Instrumentation). Agonists were kept in powder form (ATP and UDP) and dissolved/diluted at the time of experiment in daily aCSF with AF568 dye added for visualization (final concentration: 30 μM). Daily aCSF containing AF568 served as a negative control for pressure application. Red channel emission was passed through a 630 ± 75 filter (Chroma). To calculate an agonist response, a semi-automated script performed the following functions: (1) A threshold of AF568 dye spread in the red channel was used to limit the area of microglial ROI selection to cells likely encountering the agonist. (2) Within this area, an average intensity image was created of eYFP/GCaMP6s microglia from the first 30 frames (prior to agonist application) to select cells without bias toward response. A uniformly applied image threshold was used to automate microglia ROI selection using the analyze particles tool (usually representing a whole cell with soma and major processes). (3) Mean fluorescent intensities were gathered across 90 frames (30 baseline, 60 post-agonist application) for each ROI using the multi-measure tool. To calculate $\Delta F/F_0$ responses from the mean intensities, the F_0 term was set as the mean of the first 30 frames (pre-agonist application). Significant calcium responses were considered as frames in the 60s post-agonist application period which were greater than the mean $\Delta F/F$ value of the first 30 frames plus 1.5x the standard deviation of the same period. Any and all frames above this threshold were summated across the 60 frames post-agonist application to acquire the signal area ($\Delta F/F \cdot s$). For dichotomous, "responding" and "non-responding" qualifications, an ROI needed to reach a signal area value above 10 $\Delta F/F \cdot s$.

Antagonist studies

Antagonist studies utilized a paired trial design in which UDP (500 μM) was first focally applied, then an antagonist was bath applied over a 10 min period before a second UDP focal application in the identical region. Antagonists were PSB-0739 (5 μM, P2Y12 antagonist), 5-BDBD (20 μM, P2X4 antagonist), and JNJ-54175446 (10 μM, P2X7 antagonist). The antagonist effect was calculated as the overall average microglia ROI calcium response to UDP in the second (antagonist) trial divided by the first trial. Because repeated

GPCR agonism can result in desensitization, antagonist effects were compared against the effect of desensitization, established by applying UDP twice in the same region, separated by 10 min over a series of independent trials (orange bar in Figure 1E).

Characterization of UDP1.0 ex vivo

To characterize UDP1.0 sensor affinity and selectivity, a pipette containing UDP, 2-ThioUTP, ATP, or 2-MethylthioADP was used to focally apply purines/pyrimidines in the area of sensor expression at different concentrations (1 psi, 50 ms). In some trials, a longer duration of release was also performed (0.5 psi, 5 s). Florescent responses were calculated similarly to agonist calcium responses, except for a change in ROI creation. Eight square ROIs (7 × 7 μm), in a uniform configuration, were placed around the pipette tip, with the middle ROI centered on the pipette tip to acquire mean fluorescent intensities.

Validation of CalEx function

Evaluation of CalEx function was performed in naive brain slices. In control mice ($TMEM119^{2A\text{-}CreERT2}$ with tamoxifen treatment and rAAV-SFFV-DIO-GCaMP6f-WPRE-hGH-polyA transfection), 500 μM UDP was focally applied (3 psi, 200 ms) through a pipette with AF568 for visualization. Any microglial cell responding to UDP application in control tissue was analyzed using the same agonist-response analysis pipeline, except ROIs were manually created around responding cells. This was necessary because GCaMP6f transfection does not include an expression tag or produce a resting signal that is reliably detected above background levels. In CalEx mice ($TMEM119^{2A\text{-}CreERT2}$;$R26^{LSL\text{-}CAG\text{-}ATP2B2\text{-}mCherry}$), we similarly placed the UDP pipette in tissue; however, we acquired a 30 frame (1 Hz) image of the red channel at 1040 nm to clearly observe mCherry cell locations before UDP application/AF568 dye spread. We then applied 500 μM UDP from the agonist pipette in this local region. Similar to control tissue, we analyzed any cell responding to UDP application using a manual ROI for consistency. Because recombination could occur independently for CalEx-mCherry expression and GCaMP6f expression, only cells with a GCaMP6f calcium response and an mCherry signal were included for analysis in the CalEx group.

Chemotaxis studies

Chemotaxis studies were performed near L2/3 of cortex by inserting a 1 mM ATP- or UDP-containing pipette 45–60 μm into the slice with an AF568 dye in the pipette for visualization (50 μM). Process movement in *P2ry6*$^{+/+}$;$CX_3CR1^{CreER\text{-}IRES\text{-}eYFP}$;$R26^{LSL\text{-}CAG\text{-}GCaMP6s}$ and *P2ry6*$^{-/-}$;$CX_3CR1^{CreER\text{-}IRES\text{-}eYFP}$;$R26^{LSL\text{-}CAG\text{-}GCaMP6s}$ slice was visualized via the weak eYFP tag over a 20 min trial (1 Hz imaging, 150 × 150 μm area). For analysis, a 60 s frame average of the eYFP signal was gathered for each of the 20min periods. The location of the pipette tip was recorded as a fixed point in X/Y-space. Processes moving toward the pipette tip (starting from within 40 μm) were tracked per video by their bulbous tip location (in X/Y space) across the 20 average frames. The distance from pipette was calculated as the hypotenuse length formed in X/Y space from process tip to pipette tip ($a = X_{pipette}\text{-}X_{process}$; $b = Y_{pipette}\text{-}Y_{process}$; distance = $\sqrt{a^2+b^2}$). All agonists and antagonists were acquired from Tocris. Experiments were discontinued 3.5 h after slicing.

Tissue collection and RNAscope imaging

Fixed, frozen tissue was used for RNAscope imaging. Tissue was obtained following terminal isoflurane exposure, exsanguination (30 mL of ice-cold 1x PBS), and fixation (40 mL of ice-cold 10% neutral-buffered formalin (NBF). Whole brains were post-fixed in 10% NBF for 24 h at 4°C, then transferred to a 15%–30% sucrose gradient in 1x PBS at 4°C. After sinking (within 24 h), brains were placed in cryo molds, surrounded by OCT compound and frozen on dry ice. Brains were then stored in an air-tight container at −80°C until sectioning. Coronal sections containing the hippocampus were cut at 10 μm thickness on a cryostat and plated onto individual slides. Slides were stored at −80°C for less than one week before use. To perform staining, we followed the manufacturer's protocol associated with the RNAscope Multiplex Fluorescent Reagent Kit v2 (UM 323100) with the addition of a fourth channel. In one set of experiments, a *P2ry6* probe was hybridized alongside markers for brain resident cells: microglia (*Tmem119*), astrocytes (*Aldh1l1*), and neurons (*Rbfox3*, NeuN transcript). In a second set of experiments, a *P2ry6* probe was hybridized alongside markers for immune cells: microglia (*Tmem119*), $CD45^+$ (*Ptprc*), and CCR2+ (*Ccr2*). Probes were visualized by an Opal dye (Opal 520, Opal 570, Opal 620, and Opal 690) and counterstained with DAPI before being mounted with ProLong Gold. Slide imaging was performed within one week through confocal microscopy (LSM 980×, 40× magnification). Images were analyzed by an investigator blinded to the *P2ry6* channel, who (1) first established an ROI around DAPI nuclei that met cell-type assignment criteria (see Figure 1I or Figure S8B), then expanded the ROI by the pixel equivalent of 3 μm using the ImageJ "Enlarge" function. These ROIs were then mapped on to the *P2ry6* channel to obtain puncta counts and area measures. In a subset of experiments we confirmed the *P2ry6* probe was reasonably specific, due to significant signal reductions in *P2ry6*$^{-/-}$ tissue (Figure S4B). The same ROI selection and enlargement approach was then applied to naive *P2ry6*$^{-/-}$ tissue to establish *P2ry6* false inclusion levels.

Tissue collection and immunofluorescence imaging

After terminal isoflurane exposure (drop method, bell jar), mice were transcardially perfused with ice-cold 1x PBS for exsanguination (30 mL) followed by 50 mL of ice-cold 10% NBF. Whole brains were post-fixed overnight at 4°C in 10% NBF, followed by 30% sucrose in PBS for cryoprotection. Coronal sections (20 μm) were cut by a cryostat (Leica CM1520) to capture sections from dorsal to ventral hippocampus. Sections were stored at 4°C in 1x PBS containing 0.01% sodium azide. For immunofluorescent staining, sections were plated onto slides, then blocked and permeabilized for 1h using 0.4% Triton X-100 in CytoQ immuno-diluent (Vector Biosciences). Sections were then incubated overnight at 4°C with primary antibodies in CytoQ containing 0.4% Triton X-100: anti-IBA1 (1:500 Rb for Sholl analysis; 1:400 Gt for phagocytosis), anti-TMEM119 (1:300 Rb), anti-NeuN (1:500 Rb for neuron survival; 1:500 Ms for phagocytosis), anti-CD68 (1:500 Rb, 1:500 Rat), anti-LAMP1 (1:400 Rb), anti-IL-1β (1:400 Ms), and anti-cFOS (1:500 Rb). After

primary antibody incubation, sections were washed with 1x PBS. Sections were then incubated at room temperature for 1.5 h with secondary antibodies in PBS containing 0.4% Triton X-100 (1:1000, Goat or Donkey; Life Technology). Secondary antibodies were washed with 1x PBS, counterstained with DAPI (1 μg/mL, 10 min), and mounted with Fluoromount-G (Thermo).

FluoroJade-C (FJC) staining and analysis

For FJC staining, sections were plated on to slides for batch processing in 50 mL Coplin jars. Sections were first exposed to 80% ethanol with 5% NaOH, followed by 70% ethanol, then ultrapure water. Sections were blocked for 5 min with 0.04% $KMnO_4$ in water, then exposed for 20 min to FJC (0.0001% FJC working solution diluted in 1% acetic acid with 1 μg/mL DAPI). Sections were then washed and mounted with DEPEX (Electron Microscopy Sciences) for imaging. FJC staining was imaged using an EVOS FL fluorescent microscope (Thermo Fisher Scientific). Bilateral images of the CA3 pyramidal band were taken at 3 different levels (sections) of dorsal hippocampus per animal and averaged per hemisphere (10x objective, 1024× 768 pixels). Average FJC area values were established by uniform threshold and restricted to a 400 × 400 μm area centered on the pyramidal band.

Sholl analysis

Microglial Sholl analysis was performed using fixed-tissue imaging of IBA1 staining in dorsal hippocampal CA3 and somatosensory cortex. Imaging was performed with a Zeiss LSM 780 confocal microscope equipped with a 40x water-immersion objective (NA: 1.2). The DAPI channel was used to visually center the imaging field on the CA3 region or layer 2/3 of cortex, near the midline. A z stack volume was then acquired at 512 x 512-pixel resolution (212 × 212 μm) across a uniform 14 μm stack with a 1 μm step size. An average intensity image of the IBA1 channel across Z levels was then used for Sholl analysis. Sholl morphology was calculated using an ImageJ plugin,[78] with the center of the soma being user defined. Thereafter, intersections were calculated along the path of concentric circles starting 6 μm from the soma center and increasing by 1 μm in radius. Longest process length was defined by the largest concentric circle capturing a process ramification. Total intersection values were defined as the sum of all process intersections from Sholl radii for a cell.

CD68 imaging and analyses

To determine CD68 area across brain regions, sections were imaged with a Keyence BZ-X810 fluorescent microscope in the amygdala, dorsal and ventral thalamus, and hippocampus (CA3 and CA1). Images were taken from a single Z-plane (1449 × 1091 μm) with a 10x objective. A uniform threshold was applied to each image in ImageJ to determine $CD68^+$ area. CD68 expression levels in CalEx tissue were analyzed from average-intensity LSM 780 confocal z stack images (1024 x 1024-pixel resolution with 1 μm Z steps; 20x, NA:0.8). To determine CD68 expression area in CalEx-mCherry positive and negative microglia, a code performed the following steps: (1) A uniform threshold of the neutral IBA1 channel was created and established ROI outlines around IBA1 cells. (2) A uniform threshold of the CD68 channel was created. (3) Each IBA1 ROI outline is overlaid on top of the CD68 threshold image. The CD68 area captured within each IBA1 outline is recorded as the raw area and the normalized to the IBA1 outline (% area). (4) To determine if these CD68 values occur in an $mCherry^+$ or $mCherry^-$ cells, a uniform threshold of the mCherry image was taken and each IBA1 ROI was then overlaid on top of the mCherry threshold image. Any IBA1 outline which has 67% area overlap with mCherry is considered CalEx positive. Because the mCherry tag is cell-filling and can illuminate smaller microglial processes, 35–40% of microglia are counted as mCherry positive, matching recombination rates. $mCherry^-$ microglia are also clearly distinct, with 50–60% of microglia in an imaging plane having 10% or less area overlap between mCherry and IBA1. Typically, under 15% of cells fall into an intermediate range of IBA1/mCherry overlap, suggesting these criteria can effectively separate the two populations without user bias. To determine CD68 overlap with NeuN neurons in the CA3 region, a similar analysis pipeline was used. (1) A uniform threshold of the NeuN channel was created within the pyramidal band to establish individual NeuN ROI outlines. (2) A uniform threshold of the CD68 channel was created. (3) Each NeuN ROI outline was sequentially overlaid on top of the CD68 threshold image. The CD68 area captured within each NeuN outline was recorded as the raw area and the normalized (%) area of the NeuN outline. (4) The percent overlap was then segmented into no/minimal overlap (<10% area overlay), moderate interaction (between 10 and 80% overlap), and engulfment (>80% overlap). The same pipeline was applied to the IBA1 channel in place of the CD68 channel for additional analysis.

NeuN analyses

To determine neuronal cell density, NeuN sections were imaged with a Keyence BZ-X810 fluorescent microscope in the CA1 and CA3 regions of hippocampus. A single Z-plane image was taken with a 20x objective. A uniform threshold was applied to the NeuN channel and the watershed tool was used to separate overlapping nuclei. A 100 × 100 μm ROI was evenly placed over 6 different locations of the pyramidal band per image. The number of NeuN somata counted by ImageJ (analyze particles) within this ROI was averaged across the 6 sampling areas to obtain a single value per mouse. An identical approach was used to quantify Cresyl Violet staining. To determine NeuN intensity profiles in CA3, three parallel lines were drawn along the CA3 pyramidal layer (one nearer to S.R., one in the middle, and one nearer to S.O.). An intensity profile along these lines was computed using the multi-plot tool and averaged to obtain a single profile per section. These profiles are only intended for illustrative purposes in representing regions of cell loss and were not formally quantified.

Imaris rendering

Three-dimensional renderings of DAPI/NeuN/CD68/IBA1 interactions were performed by imaging a representative z stack with a 63x objective (oil, NA:1.4) and a 0.33μm step size on a Zeiss LSM 980 confocal microscope. The airy scan module was used for idealized fluorophore detection at 1884 x 1884-pixel resolution (66.5 × 66.5 μm). Rendering was performed in Imaris. IBA1 microglia and NeuN neurons were manually surface rendered, while CD68 lysosomes were represented as center-aligned spots of growing size (>0.5 μm) based upon absolute intensity.

High-parameter flow cytometry and analysis

Tissue was harvested in two cohorts, following a pilot experiment to determine panel viability and establish ideal antibody titers. Post-SE tissue was harvested 5 days after KA-SE, while a naive group was established by enrolling saline-injected sibling littermates from both genotypes in each experimental batch. After terminal isoflurane exposure, mice were exsanguinated using ice-cold 1x PBS solution to remove cell populations transiting the vasculature. The brain was rapidly removed and mechanically dissected to obtain the full cortex and bilateral hippocampi. Remaining brain tissue was utilized for staining controls. Tissue was enzymatically digested in C tubes for 30 min using the tumor dissociation kit with mild mechanical movement and heating at 37°C (Miltenyi Octo Dissociator: adult brain dissociation protocol). Tissue was further processed into a single-cell suspension following manufacturer's instructions, including steps to remove debris and myelin. Samples were then exposed to a viability dye (1:1000 Zombie UV) for 20 min at RT. Samples were washed in PBS and exposed to a surface antibody panel for 30 min at 4°C, including CD45-PerCP (1:50), CD11b-PE/Cy5 (1:100), CD126-BUV563 (1:100), MERTK-BV786 (1:100), CD25-BV750 (1:100), CX3CR1-PacificBlue (1:100), P2Y12-APC-Fire810 (1:100), TCRβ-PE/Cy7 (1:100), CD11c-SPARK-NIR-685 (1:100), Ly6G-BV711 (1:200), CD4-BV510 (1:50), CD8α-BV570 (1:50), CD122-BB700 (1:100), F4/80-BUV395 (1:200), NK1.1-BUV615 (1:100), MHCII-BUV805 (1:200). After additional wash steps, samples were fixed and permeabilized by 20 min exposure to Cytofix/Cytoperm solution (BD #554722) at 4°C. Samples were then incubated with an intracellular antibody panel for 30 min at RT in 1x permeability/wash buffer (BD #554723), including NeuN-APC (1:50), Vimentin-CL488 (1:50), TNFα-BV650 (1:100), Pro-IL1β-PE (1:50), CD68-BV421 (1:50), STING-PE/CF594 (1:50), IL2-BV605 (1:50), IFNγ-BUV737 (1:50). After a final series of wash steps, samples were kept at 4°C and analyzed within 24 h using a 5-laser Cytek Aurora spectral cytometer. For an antigen, the level of staining considered as true biological signal was established with a fluorescence-minus-one (FMO) control in which all fluorophores in the panel except for the fluorophore of interest were used in staining. Gating strategies are described in Figure S8. Due to batch-associated variability in antibody signals between cohorts, frequency calculations are normalized against the average naive value per cohort. Analyses were performed in FloJo.

Macrophage isolation and transwell assay

To obtain immune cells, C57BL6/J WT mice were injected with sterile 3% Brewer's thioglycolate medium (i.p., 1 mL). 72 h later, mice were euthanized by isoflurane and intraperitoneal cells were immediately harvested through repeated washes of the i.p. cavity with 3 mL of 1x PBS. Cells from the fluid were pelleted by centrifugation, resuspended, and magnetically labeled using the Mouse Peritoneal Macrophage Isolation Kit (Miltenyi). This kit allows for macrophage isolation by depletion of non-target cells (granulocytes, T cells, B cells, NK cells, dendritic cells, and erythroid cells) following the manufacturer's instructions. The macrophage-enriched fraction was resuspended in DMEM-F12 media containing 1% pen/strep ("serum-free media, or S.F. media) and either used for purity evaluation or a Transwell assay. For purity evaluation, 1x10^5 cells per well were plated across 4 wells of a 24-well plate, incubated for 18 h at 37°C with 5% CO_2 before fixation with 2% PFA, and staining with DAPI, IBA1 (1:750 Gt), and CD11b (1:750 Rat). For the Transwell migration/invasion assay, 1x10^5 cells were plated onto a 6.5 mm diameter mesh insert with an 8 μm pore size, seated in a 24-well plate (Corning). Beneath the transwell insert the lower well contained either S.F. media, media with serum (supplemented with 10% FBS), S.F. media with 100 ng/mL CCL2, S.F. media with 1 or 10 μM UDP, or S.F. media with 10 μM MRS-2578. Migration could occur for up to 18 h during incubation at 37°C with 5% CO_2. Thereafter, the transwell insert was carefully removed and cells that had migrated through the mesh into the lower chamber were fixed with 2% PFA, stained by DAPI, and imaged by an EVOS FL microscope. Five fields of view were randomly imaged per well (10x objective; 880× 500 μm area) and averaged to obtain 1 overall cell count per well.

Transcriptomic analysis

For bulk RNA-seq, microglia were isolated from the brains of *P2ry6*$^{+/+}$ and *P2ry6*$^{-/-}$ mice three days after KA-SE. Briefly, mice were transcardially perfused with ice-cold PBS, and the olfactory bulbs and cerebellum were removed from the brain. Remaining brain tissue was dissected into small pieces (~1 mm^3) in ice-cold PBS. Tissue was then processed by enzymatic digestion following the manufacturer's instructions (Miltenyi Adult Brain Dissociation Kit), including debris removal. Red blood cell removal was omitted due to perfusion. Single-cell suspensions were labeled with CD45-PerCP (1:100) and CD11b-BV650 (1:100) and sorted by a BD FACS Aria to obtain CD45^{Mid-Lo};CD11b^{Hi} microglia, immediately resuspended in Trizol. Isolated RNA quality was assessed with an Agilent 2100. Qualifying samples (N = 3 *P2ry6*$^{+/+}$ and N = 4 *P2ry6*$^{-/-}$) with an RNA integrity number (RIN) > 7 were processed for library preparation with the SMART SEQ II kit in a single batch. Pair-ended sequencing (PE, 100bp) was performed with the BGISEQ platform. Cutadapt was used to remove adapters from the paired-end raw reads[78]. Trimmed, paired-end reads were aligned to the mus musculus reference genome (mm10) using STAR[73] (v.2.5.4b). Evaluation of DEGs utilized the DESeq2 (v1.30.1) pipeline[74] with raw read counts estimated from STAR. The gene set provided as an initial input contained approximately 13,700 genes with a

Please cite this article in press as: Umpierre et al., Microglial $P2Y_6$ calcium signaling promotes phagocytosis and shapes neuroimmune responses in epileptogenesis, Neuron (2024), https://doi.org/10.1016/j.neuron.2024.03.017

base mean value > 0.5 to filter out virtually undetected transcripts. No other filtering was performed and default settings were used in the DESeq2 pipeline. Evaluation is presented as a WT – KO contrast, where transcripts higher in the WT mouse have a positive log_2FC value. DEGs include genes with a $log_2FC>\pm1.0$ and a $P_{adj.}>0.1$. Of note, RSEM[75] (v1.3.1) was used to calculate transcripts per million (TPM) from the .bam files generated by STAR.

Novel object recognition

Novel object recognition (NOR) tasks were performed in a cohort of *P2ry6*$^{+/+}$ and *P2ry6*$^{-/-}$ mice in a naive baseline state and one week after KA-SE. The arena consisted of a (42 × 42 × 25 cm) plexiglass box with a consistent symbol placed on each wall as a spatial cue. The entire plexiglass arena was enclosed within an insulated box providing temperature and humidity control as well as consistent lighting. Behavior was monitored by an overhead camera system. Mice were habituated to the arena for 5 min/day for 3 days preceding the baseline test. Habituation was also performed one day before the KA-SE test. The test consisted of a first "object familiarization" phase where two identical objects were placed along the center axis of the arena spaced 6.5 cm from the left ("A") and right ("B") wall. Mice were allowed to explore the arena and objects for 5 min. Mice were returned to their home cage for a 30 min period before a "novel object" phase began. In the novel object phase, a familiar object was placed in a previous location (A or B) and a novel object was placed in the other location. The identity of the novel object (between two different object sets) and the location of the novel object (A/B) was randomized across trials. Mice were given 5 min to explore the novel and familiar object in the novel object phase. The objects and arena were thoroughly cleaned with 70% ethanol after every 5 min trial. In a second NOR test performed 7 days after KA-SE (10 days after the first test), the same procedures were followed. Notably, two completely different object sets were used in the day 7 post-SE test. During the object familiarization phase, a preference index was established as the time spent exploring an object in location A divided by the time spent exploring the identical object in location B. In the novel object phase, a discrimination index was determined as the time spent exploring the novel object divided by the time spent exploring the familiar object. Exploration time was established by a consistent reviewer blinded to genotype. Exploration time was counted when mice were within 3 cm of the object and either facing the object smelling the object, or contacting the object. Bouts in which mice attempted to climb or scale the object were not counted as object exploration. Additional analysis was performed using the open-source EZtrack program to track mouse location, report overall mouse motility in a trial, and determine periods in which mice were within the novel or familiar object vicinity (by a consistent, user-defined ROI).

QUANTIFICATION AND STATISTICAL ANALYSIS

All statistical analyses were performed in GraphPad Prism. Before running statistical testing, the normality and variance of the distribution was determined to arrive on the appropriate characteristics for a statistical test. A t-test was used to compare two groups at a single timepoint. To compare two groups across time, a two-way ANOVA design was used with either a Sidak's post-hoc test (comparison between genotype/group at each time point), or a Dunnett's post-hoc test (comparison of a time point against the within-group baseline). A repeated-measures design was only used for *in vivo*, longitudinal datasets comparing the same region over time. Comparing $\geq$3 groups/categories at a single time point utilized a One-way ANOVA with either a Fisher's post-hoc test (comparison to baseline), or Tukey's post-hoc test (comparisons between all groups). All post-hoc testing accounted for multiple comparisons. A Chi-squared test compared frequency data between groups after segmenting a dataset into distinct categories. Correlations between seizure severity and outcome measures were reasonably well fit by a simple linear regression, with additional slope and intercept comparisons. Neuropathology outcomes from mice not reaching seizure inclusion criteria were processed for the sole purpose of correlational studies to achieve a wider range of outcomes. Responses to UDP across a concentration range were fit by a nonlinear log(agonist) vs. 3-parameter response equation in Prism. Sample sizes were based on prior experience using similar techniques.[3] Reduced neuropathology outcomes in *P2ry6*$^{-/-}$ mice were confirmed across two cohorts at the day 1, 3, and 7 time points, with similar findings. Experimenters were blinded to genotype for *in vivo* imaging studies, histology studies, and behavioral studies. Analysis was either performed with blinding to genotype (behavior) or using automated analysis pipelines which strongly mitigate user bias.